

**OBSERVATIONAL ANALYSIS OF TRANSIENT AND  
COHERENT STRUCTURES IN SPACE PLASMAS**

by

**JINLEI ZHENG**

**A DISSERTATION**

Submitted in partial fulfillment of the requirements  
for the degree of Doctor of Philosophy  
in  
The Department of Space Science  
to  
The School of Graduate Studies  
of  
The University of Alabama in Huntsville

**HUNTSVILLE, ALABAMA**

**2017**

In presenting this dissertation in partial fulfillment of the requirements for a doctoral degree from The University of Alabama in Huntsville, I agree that the Library of this University shall make it freely available for inspection. I further agree that permission for extensive copying for scholarly purposes may be granted by my advisor or, in his/her absence, by the Chair of the Department or the Dean of the School of Graduate Studies. It is also understood that due recognition shall be given to me and to The University of Alabama in Huntsville in any scholarly use which may be made of any material in this dissertation.

  
Jinlei Zheng

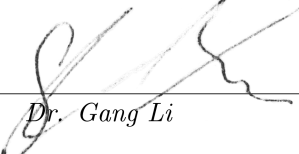
11/1/2017  
(date)

## DISSERTATION APPROVAL FORM

Submitted by Jinlei Zheng in partial fulfillment of the requirements for the degree of Doctor of Philosophy in Space Science and accepted on behalf of the Faculty of the School of Graduate Studies by the dissertation committee.

We, the undersigned members of the Graduate Faculty of The University of Alabama in Huntsville, certify that we have advised and/or supervised the candidate of the work described in this dissertation. We further certify that we have reviewed the dissertation manuscript and approve it in partial fulfillment of the requirements for the degree of Doctor of Philosophy in Space Science.

 — 11/1/2017  
Dr. Qiang Hu (Date) Committee Chair

 — 11/1/2017  
Dr. Gang Li (Date)

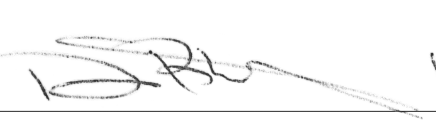
 — 11/1/2017  
Dr. Jakobus le Roux (Date)

 — 11/3/17  
Dr. Gary Zank (Date)

 — 11/02/2017  
Dr. Gary Webb (Date)

 — 11/3/17  
Dr. Gary Zank (Date) Department Chair

 — 11/07/2017  
Dr. Sundar Christopher (Date) College Dean

 — 11/12/17  
Dr. David Berkowitz (Date) Graduate Dean

## ABSTRACT

School of Graduate Studies  
The University of Alabama in Huntsville

Degree Doctor of Philosophy College/Dept. Science/Space Science  
Name of Candidate Jinlei Zheng  
Title Observational Analysis of Transient and  
Coherent Structures in Space Plasmas

---

In this dissertation, we developed a new automated small-scale magnetic flux rope detection algorithm based on the Grad-Shafranov (GS) reconstruction technique. The GS reconstruction technique is a tool to reconstruct the two and a half dimensional magnetic field and plasma structures based on in-situ spacecraft measurements in space plasmas. We applied this detection algorithm to the Wind spacecraft measurements during 1996 ~ 2016, covering two solar cycles, and successfully detected a total number of 74,241 small-scale magnetic flux rope events with durations from 9 to 361 minutes. This large number of small-scale magnetic flux ropes has not been discovered by any other previous studies through this unique approach. We have built an online database of small-scale magnetic flux ropes based on our detection results (see <http://fluxrope.info>).

We performed statistical analysis of the small-scale magnetic flux rope events based on our newly developed database, and summarize the main findings as follows. (1) The occurrence of small-scale flux ropes has strong solar cycle dependency, which has the same trend as the occurrence of their large-scale counterparts, the magnetic clouds. (2) The small-scale magnetic flux ropes in the ecliptic plane tend to align

along the Parker spiral, indicating that they belong to the general population of “flux tubes”. (3) In low speed ( $< 400$  km/s) solar wind, the flux ropes tend to have lower proton temperature and higher proton number density, while in high speed ( $\geq 400$  km/s) solar wind, they tend to have higher proton temperature and lower proton number density. (4) Both the duration and scale size distributions of the small-scale magnetic flux ropes obey a power law. (5) The waiting time distribution of small-scale magnetic flux ropes can be fitted by an exponential function (for shorter waiting times) and a power law function (for longer waiting times), suggesting the presence of both a random Poisson process and some clustering behavior. (6) The wall-to-wall time distribution obeys double power laws with the break point at 60 minutes (corresponding to the correlation length), which is consistent with the waiting time distributions of magnetohydrodynamic (MHD) turbulence simulations and the related observations. (7) The small-scale magnetic flux ropes tend to accumulate near the heliospheric current sheets (HCSs). We also performed case studies on the small-scale magnetic flux ropes downstream of interplanetary shocks, and found that the peaks of enhanced ions flux correspond to the merging edges of two adjacent flux ropes, indicating that the merging flux ropes are able to energize particles with appropriate energy bands.

In summary, we have studied an exhaustive list of small-scale magnetic flux rope structures from twenty-one-year worth of Wind spacecraft data in the solar wind. We examined their properties and related to other structures. We have found evidence supporting competing views on the origin of this type of structures. However, we conclude that we have found strong evidence in support of the mechanism of their

self-generation in MHD turbulence, especially on scales smaller than the correlation length.

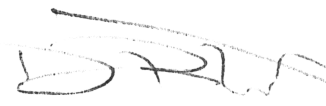
Abstract Approval: Committee Chair

  
Dr. Qiang Hu

Department Chair

  
Dr. Gary Zank

Graduate Dean

  
Dr. David Berkowitz

## ACKNOWLEDGMENTS

Firstly, I would like to express my great gratitude to my advisor, Dr. Qiang Hu, for his support and advising throughout my five and a half years study on my PhD program. He offered great encouragement during my hard time in my academic endeavor. He encouraged and supported me to attend the AGU Fall meeting, the AIAC meeting, and the NSF SHINE meeting, from which I acquired lots of valuable experience for my research. This PhD dissertation would not have been achievable without his guidance and encouragement.

I would like to thank my committee members, Dr. Gary Zank, Dr. Gang Li, Dr. Jakobus le Roux, and Dr. Gary Webb. I would like to thank Dr. Gary Zank for his kind encouragement in my research. I would like to thank Dr. Gang Li and Dr. Jakobus le Roux for the excellent courses offered by them, and also for their warm-hearted help and useful discussions. I would like to thank Dr. Gary Webb for the useful discussions, and also for his humorous talk which always makes people happy.

I would like to give my special thanks to Dr. S. T. Wu and his wife Mrs. Wu. Unfortunately, Dr. S. T. Wu passed away on May 21, 2017. He was the nicest mentor and friend I've ever met, who never stopped offering his help and encouragement in both my academic and personal life. I will never forget how happy he was and treated me to dinner when I passed my PhD comprehensive exam. I wish he would be happy to see this work.

I would like to thank CSPAR staff, Rachel, Beth, Veronica, and Sarah, who helped me a lot in the academic affairs.

I would like to give my heartfelt thanks to my grandfather, Xinlin Zheng, for his selfless love. Also give my grateful thanks to my mother Ronghua Li, and my father Gushan Zheng, for their love and encouragement throughout my life.

I would like to thank my fiancée, Lulu Zhao. She gave me many great suggestions and encouragement in both my academic and personal life.

This research intensively used the computational resource provided by the CSPAR supercomputer, the “Bladerunner”. Many thanks go to CSPAR for providing such an amazing research facility, and many thanks also go to its administrators, Dr. Jacob Heerikhuisen, Dr. Vladimir Florinski, current IT manager Justin, and the former IT manager Brian.

This PhD study would not have been possible without many funding supports. My advisor and I gratefully acknowledge the following grants for partial support: NASA grants NNX12AH50G, NNX14AF41G, and NRL contract N00173-14-1-G006 (NASA prime: NNH13ZDA001N); NSF grants AGS-1062050, and AGS-1650854. I also gratefully acknowledge the graduate assistantships offered by the Physics Department and the Space Science Department, at the University of Alabama in Huntsville.

My advisor and I also acknowledge useful discussions with Drs. Pete Riley and Mark Linton on the development of the automated detection of flux ropes by the GS method.

I would like to thank the data providers. The ACE spacecraft data are accessed from the ACE Science Center and the NASA CDAWeb. The Wind spacecraft data

are retrieved from the NASA CDAWeb. The interplanetary shock list is from the Heliospheric Shock Database, generated and maintained at the University of Helsinki. The HCSs crossings are from Leif Svalgaard's IMF sector boundary list. The sunspot numbers are obtained from WDC-SILSO, Royal Observatory of Belgium, Brussels.

## TABLE OF CONTENTS

<b>List of Figures</b>	<b>xiii</b>
<b>List of Tables</b>	<b>xxii</b>
<b>Chapter</b>	
<b>1 Introduction</b>	<b>1</b>
1.1 Overview: Structures and Transients in the Solar Wind . . . . .	1
1.2 Magnetic Flux Ropes . . . . .	6
1.2.1 Large-scale Magnetic Flux Ropes: Magnetic Clouds . . . . .	9
1.2.2 Small-scale Magnetic Flux Ropes . . . . .	11
1.3 Research Objectives . . . . .	16
1.4 Research Methodology . . . . .	18
1.5 Organization of This Dissertation . . . . .	21
<b>2 Grad-Shafranov Reconstruction Technique</b>	<b>22</b>
2.1 Introduction . . . . .	22
2.2 Two-dimensional Magnetohydrostatic Equilibrium . . . . .	23
2.3 Field Line Invariants . . . . .	24
2.4 The Grad-Shafranov Equation . . . . .	27
2.5 GS Reconstruction Examples . . . . .	30
2.5.1 CASE 1: Wind 2002/2/1 00:25 ~ 03:15 UT . . . . .	33

2.5.2	CASE 2: Wind 2002/2/1 10:36 $\sim$ 12:55 UT	35
2.5.3	CASE 3: Wind 2002/2/1 14:57 $\sim$ 17:03 UT	36
<b>3</b>	<b>Automated Detection Algorithm Based on the GS Method</b>	<b>38</b>
3.1	Automated Detection Algorithm	41
3.2	Cleanup and Post-Processing	50
3.3	Online Database of Small-scale Magnetic Flux Ropes	55
<b>4</b>	<b>Small-scale Magnetic Flux Rope Database and Statistical Analysis</b>	<b>61</b>
4.1	Occurrence Rate of Small-scale Magnetic Flux Ropes	61
4.2	Axial Orientations of Small-scale Magnetic Flux Ropes	68
4.3	Statistical Properties of Small-scale Magnetic Flux Ropes	72
4.4	Waiting Time Distribution Analysis on Small-scale Magnetic Flux Ropes	86
4.5	Locations of Small-scale Magnetic Flux Ropes with Respect to the Heliospheric Current Sheet (HCS)	98
<b>5</b>	<b>Association between Small-scale Magnetic Flux Ropes and Inter- planetary Shocks</b>	<b>106</b>
5.1	Introduction	106
5.2	Case Studies	111
5.2.1	CASE 1: 1999/3/9 23:40 UT $\sim$ 1999/3/10 09:40 UT	112
5.2.2	CASE 2: 2003/12/7 12:41 UT $\sim$ 2003/12/7 22:41 UT	120
5.3	Summary and Discussion	126
<b>6</b>	<b>Conclusions</b>	<b>128</b>

6.1	Summary of Work in This Dissertation . . . . .	128
6.2	New Results in This Dissertation . . . . .	131
6.3	Future Work . . . . .	134
<b>REFERENCES</b>		<b>137</b>

## LIST OF FIGURES

2.1 Time series data from 2002 Jan. 31, 00:00 UT to 2002 Feb. 2, 00:00 UT. This time interval contains one interplanetary shock and three flux rope structures. The first panel is the magnetic field data from Wind. The black solid line denotes the total magnetic field magnitude. The second panel is the solar wind bulk speed from Wind. In the third panel, the proton number density is shown in blue line and the alpha/proton ratio is shown in green line. These two sets of data are from Wind. The fourth panel are the proton temperature (in blue line) and plasma beta (in green line), both of which are from Wind. The proton temperature (in $10^6$ K) was calculated from proton thermal speed, and the plasma beta was calculated from proton number density, proton temperature, and the magnetic field. The contribution of electrons to plasma beta was not taken into account, because there was no electron temperature data available. The shock is denoted by a vertical black dashed line. The time of this shock is 2002 Jan. 31, 21:38 UT. The shaded regions represent three small scale flux ropes, which are labeled as CASE 1, CASE 2 and CASE 3, respectively. . . . .	32
2.2 GS reconstruction result for CASE 1 (2002 Feb. 1, 00:25 - 03:15 UT). (a) The cross-section magnetic field configuration of the flux rope. The unit vector $\hat{\mathbf{z}}$ represents the $z$ -axis orientation of the flux rope in GSE coordinates. The filled color contour represents the axial magnetic field $B_z$ and the line contour overlapped in black represents the transverse magnetic field lines. The white dot in the center is the location of the maximum axial field $B_z$ . The white arrows across the map horizontally are projected transverse magnetic field vectors along the spacecraft path. The white contour line encloses the region $A > A_b$ , denoted in (b). The reconstruction map within this line is reconstructed by double-folded $P_t(A)$ data, and the region beyond this line is reconstructed based on the extrapolated data. (b) The fitting curve (bold solid line) of $P_t(A)$ for CASE 1. The fitting is based on the data points marked by blue circles and red stars, where the circles represent the data as spacecraft was crossing the first half of the flux rope structure and the stars represent those of the second half. The thin vertical solid line denoted by $A_b$ marks the boundary corresponding to the white contour line in Figure 2.2(a). . . . .	34
2.3 GS reconstruction result for CASE 2 (2002 Feb. 1, 10:36 - 12:55 UT). The format is the same as in Figure 2.2. . . . .	35
2.4 GS reconstruction result for CASE 3 (2002 Feb. 1, 14:57 - 17:03 UT). The format is the same as in Figure 2.2. . . . .	36

3.1	Flux rope detection algorithm flowchart. A rounded rectangle represents the beginning or end of a loop; a rectangle represents a process; a diamond represents a conditional judgement; and a parallelogram represents data input or output. The core loop is enclosed by the dashed lines. . . . .	44
3.2	The home page of the small-scale magnetic flux rope database website. . . . .	56
3.3	The annual event list page of the small-scale magnetic flux rope database website. . . . .	57
3.4	Detailed information for one small-scale magnetic flux rope record: event page part 1. . . . .	58
3.5	Detailed information for one small-scale magnetic flux rope record: event page part 2. . . . .	59
4.1	(a) The monthly counts of flux rope events occurrence (left axis) and the monthly sunspot number (black curve; right axis) during 1996-2016. Colors represent counts of events with different durations as indicated by the legend in minutes. (b) The monthly flux rope total duration (left axis) and the monthly sunspot number (right axis) during 1996-2016. The format is the same as in (a). . . . .	62
4.2	The upper panel is small-scale flux rope occurrence counts per month of observation for 1974 ~ 2006. The lower panel is the monthly occurrence counts averaged over solar cycles 21 to 23. Gray curves show the corresponding sunspot numbers. (Credit: Cartwright and Moldwin [72]).	64
4.3	Occurrence counts of magnetic clouds, frontside halo CMEs and the sunspot number from 1996 to 2014 (Credit: Gopalswamy et al. [131]).	67
4.4	(a) Flux rope axial orientation: polar angle $\theta$ histogram. The actual polar angle range is from $0^\circ$ to $180^\circ$ . To cut down the time consumption in flux rope detecting process, we restrict the end points of the direction vectors to be in the upper hemisphere, and do not distinguish the vectors with opposite directions from each other. (b) Flux rope axial orientation: azimuthal angle $\phi$ histogram. This angle is measured from the positive GSE $X$ -axis toward the projection of the flux rope axis onto the ecliptic plane. . . . .	69

4.5 The scatter plots of three-dimensional unit vector tips of 65,860 flux tube axes observed by the ACE spacecraft in the solar wind by Borovsky et al. [104]. The time range is from the year 1998 to 2004. The three-dimensional vector tips plotted in top panels are in $r$ versus $-t$ coordinates, and the three-dimensional vector tips plotted in bottom panels are in a coordinate system $(r', t', n)$ with $r'$ along the nominal Parker spiral direction. The 2nd to 98th percentiles range of values of the expected Parker spiral directions are indicated as the short curves labeled “P.S.” (Credit: Borovsky et al. [104]). . . . . .	70
4.6 A depiction of the flux tube structure of the solar wind proposed by Borovsky et al. [132] (Credit: Borovsky et al. [132]). . . . .	71
4.7 The histogram of average solar wind speed within small-scale flux ropes. . . . .	73
4.8 The 2-D histogram of flux rope average solar wind speed ( $\bar{V}_{sw}$ ) versus scale size. . . . .	74
4.9 (a) The histogram of small-scale flux rope duration plotted in logarithmic scales. The time range is from 9 minutes to 361 minutes, with 5 minutes bin size. Note that the high tails to the right ends of the curves are due to duration boundary cutoff effect (see explanations in text). (b) The histogram of small-scale flux rope cross section scale sizes plotted in logarithmic scales, with 0.00025 AU bin size. The flux rope scale size is calculated from the flux rope duration taking into account the axial orientation. Again, the low points to the left and right ends of the curves are due to boundary cutoff effect. For both (a) and (b), the basic statistical properties and linear regression parameters for each curve are listed, respectively. . . . .	75
4.10 The 2-D histogram of flux rope scale size versus duration. The bin grids are $100 \times 100$ . Subplots (a) to (e) are histograms under different solar wind speeds, and subplot (f) is the histogram for the entire dataset. The color bar represents the corresponding small-scale flux rope counts. . . . .	78
4.11 (a) The histogram of average proton temperature within flux ropes in logarithmic scales, with $0.005 \times 10^6$ K bin size. (b) The histogram of average proton number density within flux ropes in logarithmic scales, with 0.2 #/cc bin size. For both (a) and (b), the blue curve represents the flux rope events under solar wind speed $\bar{V}_{sw} < 400$ km/s, and the red curve with solar wind speed $\bar{V}_{sw} \geq 400$ km/s. The black curve represents the entire event set. . . . .	81

4.12 (a) The histogram of average plasma $\beta$ within flux ropes, with bin width 0.01. (b) The histogram of average proton plasma $\beta_p$ within flux ropes, with bin width 0.01. For both (a) and (b), the blue curve represents the flux rope events with solar wind speed $\bar{V}_{sw} < 400$ km/s, and the red curve with solar wind speed $\bar{V}_{sw} \geq 400$ km/s. The black curve represents the entire event set. . . . .	83
4.13 The 2-D histogram of flux rope proton temperature <i>versus</i> scale size. The bin grids are $200 \times 200$ . Subplots (a) to (e) are histograms under different solar wind speeds, and subplot (f) is the histogram for the entire dataset. The color bar represents the small-scale flux rope counts. . . . .	85
4.14 The waiting time distribution (1st kind) of small-scale magnetic flux ropes. In this plot, the waiting time is defined by the interval between the end time of one flux rope to the start time of the next one. The dots in black represent the entire data set, and the dots in blue and red represent the subsets under low solar wind speed ( $\bar{V}_{sw} < 400$ km/s) and medium as well as high solar wind speed ( $\bar{V}_{sw} \geq 400$ km/s), respectively. The bin size is 5 minutes, and the data point for each bin is located in the bin center. The dashed lines are fitted curves by exponential functions, and the solid lines are fitted curves by power law functions. The dotted vertical line denotes the break point, which is located at 60 minutes. The basic statistics and fitting parameters are denoted, where the function forms and the fitting quality metric $R^2$ are listed. . . . .	88
4.15 The waiting time distribution (2nd kind) of small-scale magnetic flux ropes. In this plot, the waiting time is defined by the interval between the start time of one flux rope to the start time of the next one. The format is the same as in Figure 4.14. The vertical dotted line is at 80 minutes. . . . .	89
4.16 The wall-to-wall time distribution of small-scale magnetic flux ropes. The walls correspond to flux rope boundaries. Format is the same as Figure 4.14. The dashed lines and the solid lines are all fitted by power law functions with different power indices. The dotted vertical line denotes the break point, which is located at 60 minutes. . . . .	92
4.17 PDF of the axial electric current density inside the small-scale magnetic flux ropes derived from our database. The original current density values are binned by $0.01 \times 10^{-9}$ Ampere/m <sup>2</sup> . The three black curves with different markers are normalized by different multiples of the standard deviation. The blue curve is the standard Gaussian distribution. This PDF takes into account all small-scale flux ropes, including the ones with average magnetic field magnitude less than 5 nT. . . . .	95

4.18 PDF of the out-of-plane electric current density $J_z$ from the 2-D simulation, compared to a reference standard Gaussian distribution. The colored (red) regions in subfigures I, II, and III are places where the selected band (I, II, or III) corresponds to. Region I: very low values of fluctuations that lie mainly in the lanes between magnetic islands. Region II: current cores of central regions of magnetic islands. Region III: small-scale current sheet-like structures that form the sharp boundaries between the magnetic islands. (Credit: Greco et al. [97]). . . . .	96
4.19 Small-scale flux rope distribution with respect to the time to the nearest heliospheric current sheet. The events are binned by 1 day. Negative value means the time ahead of the HCS. The red and blue curves represent the events occurring under different solar wind speed conditions (blue curve: $\bar{V}_{sw} < 400$ km/s, red curve: $\bar{V}_{sw} \geq 400$ km/s). . . . .	99
4.20 Annual small-scale flux rope counts distribution with respect to the nearest heliospheric current sheet. The events are binned by 1 day. Negative days mean the occurrence time ahead of HCS. . . . .	101
4.21 The 2-D histograms of flux rope average proton temperature <i>versus</i> time to the nearest HCS. The <i>x</i> -aixs is binned by 1 day. Negative values mean the time ahead of HCS. Subplots (a) to (e) are histograms under different solar wind speeds, and subplot (f) is the histogram for the entire dataset. The color bar represents the small-scale flux rope counts. . . . .	103
4.22 The 2-D histograms of flux rope average proton number density <i>versus</i> time to the nearest HCS. The format is the same as in Figure 4.21. . .	104
5.1 (a) The monthly counts of flux rope events occurrence (left axis) and the monthly sunspot numbers (black curve; right axis) during 1996-2016. Colors represent counts of events with different durations as indicated. Green solid curve shows the yearly shock number observed by Wind spacecraft. (b) The monthly flux rope total duration (left axis) and the monthly sunspot numbers (right axis) during 1996-2016. The format is the same as in (a). For both (a) and (b), all the flux ropes are downstream of shocks (within 12 hours downstream from the shock time). . . . .	108



5.6 GS reconstruction result for flux rope record No.7 (March 9th, 1999, 05:28 - 05:46 UT) in Figure 5.3. (a) The cross-section magnetic field configuration of the flux rope. The unit vector $\hat{\mathbf{z}}$ represents the $z$ axis orientation of the flux rope. The filled color contour represents the axial magnetic field $B_z$ and the line contour overlapped in black represents the transverse magnetic field. The white arrows across the map horizontally are projected transverse magnetic field vectors along the spacecraft path. The white contour line encloses the region $A < A_b$ in this case (within the flux rope boundary $A = A_b$ , denoted in (b)). The reconstruction map within this line is reconstructed by the double-folded spacecraft data, and the region beyond this line is reconstructed based on the extrapolated data. (b) The fitting curve (bold solid line) of $P_t(A)$ for this flux rope case. The fitting is based on the data points denoted by blue circles and red stars, where the circles represent the data sampled as the spacecraft crossed the first half of the flux rope structure and the stars represent those of the second half. The thin vertical solid line denoted by $A_b$ marks the boundary corresponding to the white line in (a). A fitting residue $R_f$ is also denoted. . . . .	117
5.7 GS reconstruction result for flux rope record No.8 (March 9th, 1999, 05:49 - 06:10 UT) in Figure 5.3. The format is the same as Figure 5.6. . . . .	118
5.8 GS reconstruction result for the combination of flux ropes No.7 and No.8 (March 9th, 1999, 05:28 - 06:10 UT) in Figure 5.3. The format is the same as Figure 5.6. . . . .	118
5.9 GS reconstruction result for the flux rope record No.7 (March 9th, 1999, 05:49 - 06:10 UT) in Figure 5.4. The format is the same as Figure 5.6. . . . .	120
5.10 Time series data (ACE) from Dec. 7, 2003, 12:41 UT to Dec. 7, 2003, 22:41 UT. The format is the same as Figure 5.3. . . . .	121
5.11 Time series data (Wind) from Dec. 7, 2003, 12:00 UT to Dec. 7, 2003, 21:00 UT. The format is the same as Figure 5.4. . . . .	122
5.12 The positions of ACE and Wind spacecraft in the GSE coordinate system. The left panel is the projection on the XY-plane, and the right panel is the projection on the XZ-plane. Both time stamps of ACE and Wind are July 12th, 2003, 16:00 UT. The unit of all axes is Earth radius. . . . .	123
5.13 GS reconstruction result for flux rope record No.3 (2003 Dec. 7, 15:29 ~ 16:41 UT) in Figure 5.10. The format is the same as Figure 5.6. . .	124

5.14 GS reconstruction result for flux rope record No.5 (2003 Dec. 7, 17:18  
- 18:08 UT) in Figure 5.11. The format is the same as Figure 5.6. . . 125

## LIST OF TABLES

TABLE	PAGE
3.1 Small-scale Magnetic Flux Rope Detection Metrics and Criteria . . .	55
3.2 The Number of Detected Small-scale Magnetic Flux Ropes in Each Year	55

*Dedication*

*To my parents, for all of their love, support, encouragement, and dedication.*

*To my grandparents, for all of their far-reaching love beyond generations.*

*To my fiancée, for all of her love, help, and encouragement.*

# CHAPTER 1

## INTRODUCTION

### 1.1 Overview: Structures and Transients in the Solar Wind

Solar wind is the stream of plasma composed of fully ionized gas, mostly protons and electrons. The solar wind originates from the atmosphere of the Sun, the corona, and travels radially outward, carrying along the solar magnetic field, until it reaches the region where the local interstellar medium has the counterbalance pressure. The theory for the supersonic solar wind plasma was first proposed by Parker in 1958 [1]. Later the existence of the fast solar wind outflow predicted by Parker's theory was confirmed by in-situ spacecraft observations. Nowadays, solar wind has become the major research topic in space physics as the characteristics and variability of the solar wind, and their impact on the whole heliosphere, the cavity carved out by the solar wind, is not well understood.

The drastic solar activities engender plasmas with various characteristics in terms of speed, magnetic field, elemental components, different particle energy, and thermal, as well as non-thermal properties, which make the solar wind always undergo large variations over a wide range of scales. The long-term variation of solar activity is called solar cycle. The solar cycle has a 11-year period as indicated by the number

of sunspots. There are two extreme periods or phases in one solar cycle, namely, the solar minimum and the solar maximum. The solar wind shows much different properties during solar minimum and solar maximum. Figure 1.1 shows the classical solar wind speed distribution as a function of latitudes around the Sun during the solar minimum (left) and the maximum (right) [2], respectively. This plot shows that during solar minimum, the solar wind speed near the low-latitude equatorial region is relatively low, while the solar wind speed near the poles is relatively high. The transition between the slow and fast wind regions is clear, usually located near  $\pm 35^\circ$  latitudes. Correspondingly, the positive and negative polarities of the magnetic field in the northern and southern hemispheres are well separated. The two polarities are well separated by the heliospheric current sheet (HCS). The heliospheric current sheet (HCS) is considered the largest structure in the heliosphere [3–8]. Figure 1.2 (a) is an artistic rendering of the heliospheric current sheet, so-called “ballerina’s skirt”, extending beyond the Earth’s orbit in the solar system. The magnetic polarity above the HCS is opposite to that below it, corresponding to Figure 1.1, top left. On the other hand, during solar maximum, both the solar wind speed distribution and magnetic polarities are irregular. The fast and slow wind streams, as well as the magnetic field polarities, are intermixed.

On relatively short time scales, the plasma dynamic processes usually occur when different plasma regimes interact with each other, forming some special structures and transients. Two examples of plasma interactions in the solar wind are interactions between fast and slow solar wind streams, forming corotating interaction regions (CIRs) [9–18], and the interaction between the coronal mass ejections

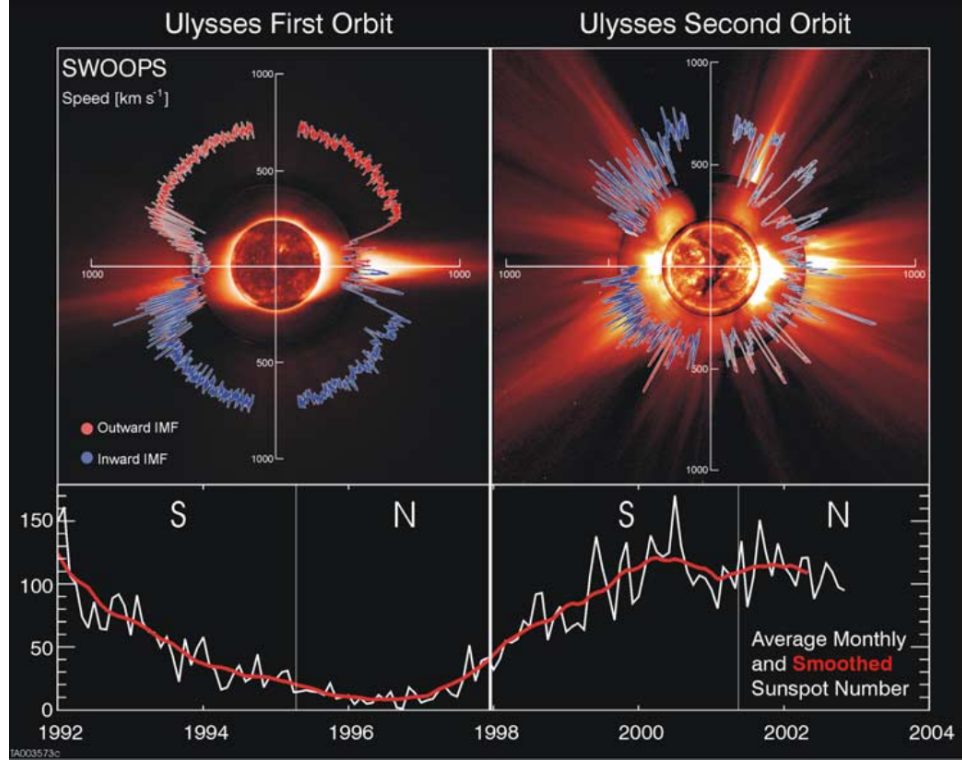


**Figure 1.1:** Polar plots of solar wind speed measured by the Ulysses spacecraft over all latitudes during the solar minimum (1992  $\sim$  1998, upper left) and the solar maximum (1998 onward, upper right). The corresponding sunspot number variation is shown in the bottom panel. The red and blue colors represent outward and inward polarities of the solar wind magnetic field, respectively. Plot adopted from McComas et al [2].

(CMEs) and the ambient solar wind, forming interplanetary coronal mass ejections (ICMEs) [19–21]. When collision between two plasmas occurs, current sheets or discontinuities are generally produced and act as boundaries (or “walls”) to separate different plasma regimes. If the relative speed between the two plasma regimes is supersonic, collisionless shocks will be generated at the leading and/or trailing interaction boundary [22–24]. Figure 1.2 (b) illustrates the overall scenario and various structures and processes embodied surrounding a CIR region. The schematic shows

that a compression region is formed where the fast solar wind overtakes the slow solar wind due to the rotation of the Sun. A pair of shocks may form at the front and back edges when the structure evolves to larger radial distances from the Sun.

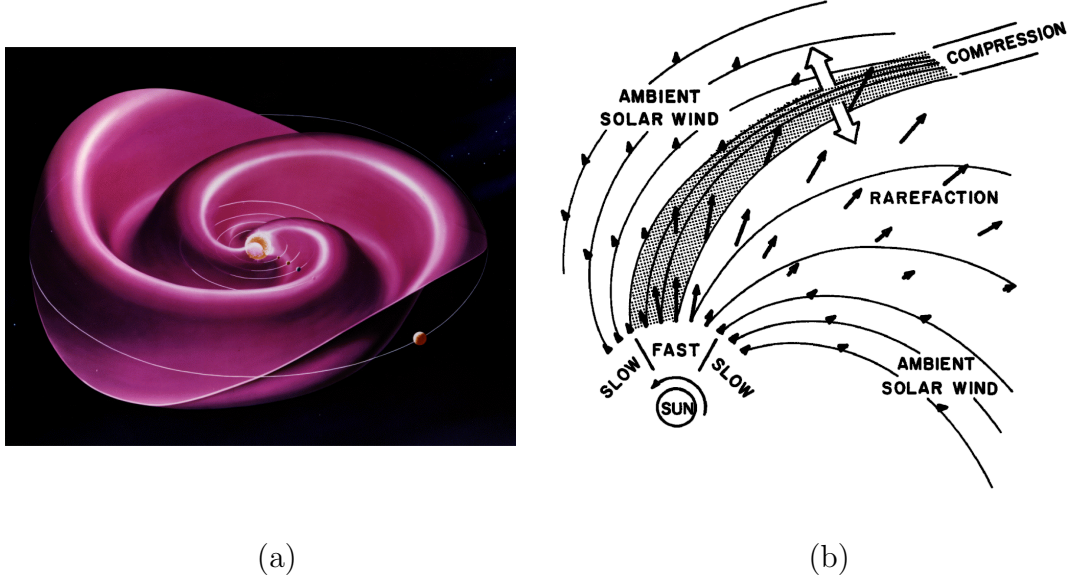


**Figure 1.2:** (a) A heliospheric current sheet (HCS) cartoon painted by NASA artist Werner Heil, developed by Dr. John Wilcox. (b) A co-rotating interaction region (CIR) schematic suggested by Pizzo et al. [14].

Figure 1.3 shows an ICME schematic suggested by Zurbuchen and Richardson [25]. In this schematic, the body of a CME has a large-scale magnetic structure, so-called magnetic cloud, embedded (see Section 1.2.1). The two roots of the magnetic cloud are connected to the Sun, and the twisted field lines are winding around the axis throughout the entire structure. A shock is formed in front of the leading edge of the magnetic cloud. The counterstreaming electrons are traveling along the field lines from the Sun. Such a complex system of structures and multiple dynamic processes often gives rise to the generation of small-scale structures, including current sheets,

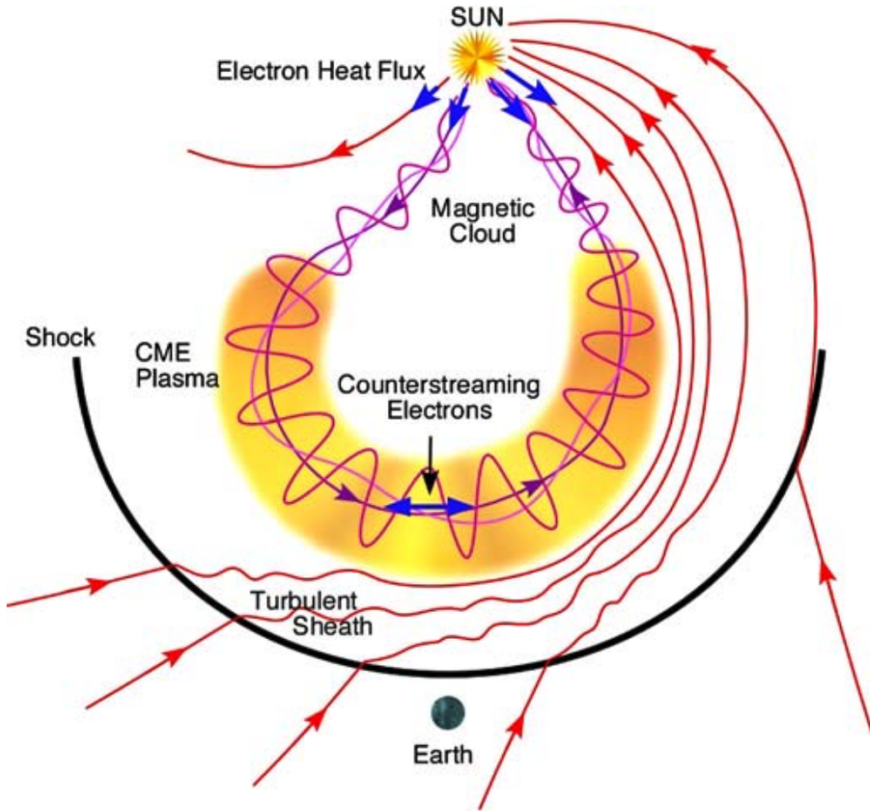


**Figure 1.3:** An ICME schematic suggested by Zurbuchen and Richardson [25].

vortices, and plasmoids (or flux ropes) due to turbulence dynamics and similar driving forces such as shear flows. These small-scale structures may be detected in ambient solar wind, near HCS and CIRs, and downstream of shocks, in the sheath region of enhanced turbulence. Besides HCS, CIRs, CMEs, and collisionless shocks, magnetic flux ropes are another important and ubiquitous type of structures in the heliosphere. They are closely related to the other structures and often exhibit properties akin to both coherent and transient structures in magnetized plasmas. Magnetic flux ropes of different scale sizes are extensively observed and studied in a variety of space plasma

environment, including the solar wind, solar active regions, the magnetotail, and the Martian atmosphere [26].

Because the formation, propagation and evolution of these structures and transients are essential intermediate steps during the space plasma dynamic processes which lead to energy and momentum redistribution, studies on these structures and transients are critical to the understanding of the entire space plasma dynamics. Some structures and transients, such as the CMEs, CIRs, current sheets, collisionless shocks, and the large-scale magnetic flux ropes, have been extensively studied in the past decades. However, for the small-scale magnetic flux ropes in the solar wind, many questions remain. Do they have the same origin as the large-scale flux ropes? How do they evolve and propagate? What are the relations between small-scale flux ropes and interplanetary shocks, current sheets, and particle energization? This dissertation focuses on the study of these small-scale magnetic flux ropes in the solar wind and their inter-relation with other structures. We build a comprehensive small-scale flux rope database via the Grad-Shafranov(GS) reconstruction technique, and carry out the statistic analysis as well as case studies to address the essential questions on the small-scale flux ropes.

## 1.2 Magnetic Flux Ropes

A magnetic flux rope is defined by its magnetic field configuration, generally regardless of the associated plasma profile and generation mechanism. In terms of the magnetic field configuration, a magnetic flux rope has the following characteristics: the topology of the magnetic field has the helical structure, in which the field

lines are winding around a central axis, forming the helix shape elongated along the axial dimension. In a locally two-dimensional (2-D), i.e., cylindrical geometry, if we align the axis of a flux rope along the  $z$ -axis in a Cartesian coordinate system, the magnetic field component along the axial direction ( $B_z$ ) generally reaches its maximum magnitude on the central axis, and decreases with increasing distance from the central axis. Meanwhile, the transverse component (perpendicular to  $z$ -axis) is zero on the central axis and varies with increasing distance from the central axis. As a result, the twist of helical magnetic field lines changes from the center of the flux rope outwards. The total magnetic field strength is usually elevated throughout the flux rope interval, compared with the field strength in the ambient medium. With such a magnetic field configuration described above, as a spacecraft passes through the helical field lines of a magnetic flux rope, the in-situ data of magnetic field vectors will show a smooth and continuous rotation in direction. Strictly speaking, magnetic flux ropes are not always in cylindrical shape. They may take toroidal or more complicated shapes on large scales beyond a local spatial domain confined in the vicinity of a single-spacecraft path.

Practically, many structures with the magnetic field configuration defined above, but with different plasma profiles, generation mechanism, and scale sizes, are simply referred to as magnetic flux ropes. The concept of magnetic flux rope is widely used to interpret a number of phenomena in the solar-terrestrial physics. As early as 1960s, Gold and Hoyle [27] suggested a twisted magnetic structure to answer the question on how energy is stored and suddenly released during solar flares. In 1981, Burlaga et al. [28] analyzed the plasma flow behind an interplanetary shock,

and found that there is a region with smooth rotation of magnetic field vectors and low proton temperature. They called this region magnetic cloud that usually lasts for a dozen hours to days in duration. Magnetic clouds (MCs) are believed to be the manifestation of corona mass ejections (CMEs). In 1989, Priest et al. [29] proposed a twisted magnetic flux tube to model solar prominences. It is widely accepted that the solar active regions contain large magnetic flux ropes. In the corona, the magnetic flux ropes could either pre-exist below photosphere before solar eruption, emerging buoyantly through the convection zone [30–38], or form from the sheared arcade in corona by magnetic reconnection [39–43]. Magnetic flux ropes are also found in Earth’s magnetopause and magnetotail. They often correspond to the so-called flux transfer events (FTEs) in the dayside magnetopause and plasmoids in the tail. In the tail, these flux ropes are believed to be generated by multiple reconnections across the magnetotail current sheet [44–51]. Another distinct population of magnetic flux ropes observed in the solar wind has much smaller scale sizes compared to magnetic clouds [52, 53]. Moldwin et al. [53] suggested that these small scale flux ropes are formed by magnetic reconnection across the heliospheric current sheet (HCS). They may possess distinct set of features from their large-scale counterparts, the magnetic clouds.

As seen above, the magnetic flux ropes are ubiquitous in the solar system. In this dissertation, we mainly focus on the magnetic flux ropes in the solar wind. In the context of the solar wind, magnetic flux ropes are empirically categorized into large-scale magnetic flux ropes (i.e., magnetic clouds) and small-scale magnetic flux ropes according to the scale sizes of their cross sections. The large-scale magnetic flux

ropes usually take the form of magnetic clouds and are extensively studied. However, the small-scale magnetic flux ropes are less studied and not well categorized. In addition to the difference in scale sizes, it is possible that small-scale magnetic flux ropes are also different in terms of origination, formation mechanism, plasma profile, and evolution process, compared with their large-scale counterparts.

### 1.2.1 Large-scale Magnetic Flux Ropes: Magnetic Clouds

The large-scale magnetic flux ropes are equivalent to the magnetic clouds (MCs) in the solar wind. The large scale magnetic flux ropes with a duration of about half a day to a few days at 1 AU in the solar wind are usually referred to as magnetic clouds. The scale sizes of magnetic clouds range from  $\sim 0.1$  AU up to 0.4 AU in diameter at 1 AU heliocentric distance from the Sun. The magnetic cloud was first identified by Burlaga et al. [28] in the solar wind between the heliocentric distances 1 AU and 2 AU. The spacecraft traversed a region with a radial dimension of 0.5 AU (0.25 AU in radius), in which the measured magnetic field vectors rotated nearly parallel to a plane. In this region, the magnetic pressure dominated and the total pressure was higher than that outside. Magnetic clouds are well defined observationally as a magnetic structure possessing these three bulk properties based on in-situ magnetic and plasma measurements: enhanced magnetic field strength, smooth rotation in the magnetic field direction, and low proton temperature. They have been intensively studied in the past decades. It is widely accepted that the magnetic clouds have the following characteristics based on the analysis and modeling of in-situ spacecraft measurements: (1) the topology of magnetic field is that of a

helical structure, in which the field lines are winding around a central axis, forming the helix shape elongated along the axial dimension. As a spacecraft passes through the helical field lines of a flux rope, the in-situ data of magnetic field vectors show a smooth and continuous rotation with variable degree of field-line twist [26]. (2) The magnetic field in a magnetic cloud is stronger than the surrounding solar wind, and the magnetic pressure usually dominates. (3) The proton temperature is depressed within the magnetic cloud, resulting in ultra-low proton  $\beta$  value, the ratio between the proton plasma and magnetic pressure. Besides these key properties mentioned above, magnetic clouds have a typical radial scale size reaching a few tenths of an AU at 1 AU [54]. A limited number of studies also examined their radial evolution between 0.3 and 4.2 AU [55]. They also clearly have a solar origin, corresponding to CMEs, often with accompanying solar flares and prominence eruptions [26].

Observational evidence suggested that the magnetic clouds have a close relation to the coronal mass ejections (CMEs) [56–60]. The CMEs interact with ambient solar wind when they are propagating into the heliosphere. Because the CMEs generally move faster than the ambient solar wind, when they become the interplanetary coronal mass ejections (ICMEs), they often drive shock waves. At least a subset of ICMEs has the properties of magnetic clouds as detected by a single spacecraft [61]. The fraction of MCs among ICMEs has a solar activity cycle dependence [62]. From the studies of 56 magnetic clouds at 0.7 AU during 1979-1988, Mulligan and Russell [63] showed that the leading magnetic field in magnetic clouds was controlled by the solar global field. The studies by Lynch et al. [64] suggested that the net accumulative helicity of most magnetic clouds appeared to be modulated by solar activity

cycle. The radial scale size of magnetic clouds expands as they move outward from the Sun [28, 57, 65–68]. Besides the radial expansion, a significant poloidal motion was also found in some magnetic clouds [68]. It is also observed that the passage of ICMEs/MCs near Earth often leads to noticeable and prolonged decrease of cosmic ray levels on the ground, a well-known phenomenon called “Forbush decrease”.

### 1.2.2 Small-scale Magnetic Flux Ropes

The small-scale magnetic flux ropes have the magnetic field configuration similar to large-scale flux ropes, i.e. MCs. However, most of them have much smaller scale sizes ranging from  $\lesssim 0.001$  to  $\sim 0.01$  AU at 1 AU heliocentric distance from the Sun, and the identification of small-scale flux ropes is less definitive. Unlike MCs which have a clear association with CMEs, originating from solar corona, the origin of small-scale flux ropes is still debatable. Some non-solar source magnetic flux ropes appear to be created by magnetic reconnection in local plasma environment, such as those by magnetic reconnection across the plasma sheet in the magnetotail. Some small-scale flux ropes in the solar wind may share the same generation mechanism.

The concept of small-scale magnetic flux ropes in the solar wind was first introduced by Moldwin et al. [53]. They observed some flux ropes with smaller sizes compared with MCs in the solar wind, while the former had durations of tens of minutes as opposed to a number of hours to days for MCs. They suggested that these small-scale flux ropes were products of magnetic reconnection in the solar wind, instead of in the solar corona. Moldwin et al. [52] reported a non-CME flux rope at 5 AU. The scale size of that flux rope was about 0.05 AU, and the plasma profile was

different from that of magnetic clouds. They interpreted this flux rope as a result of multiple magnetic reconnection at the heliopsheric current sheet (HCS).

In recent years, small-scale flux ropes have attracted interest of some researchers as they started to compare the different characteristics of small-scale flux ropes with MCs. Feng et al. [69] identified 144 magnetic flux ropes with radial scale sizes from about 0.0039 to 0.6266 AU (including both large and small scale flux ropes). Based on the similarity of their energy distributions to solar flares, they suggested that the small-scale and intermediate-scale flux ropes were the interplanetary manifestations of some small CME events. On the other hand, Cartwright and Moldwin [70] identified 68 flux ropes with strong core field using Wind spacecraft magnetic field data. They excluded the possible macroscale Alfvén waves in the identification. The duration ranged from 39 minutes to 12.2 hours. The comparison showed that these two types of flux ropes differ in terms of expansion, whether or not in force-balance, the strengths of core fields, and the association with forward shocks, which implied that they may have different origins. Feng et al. [71] surveyed 125 small-scale and intermediate-scale flux ropes. They suggested that the small-scale and intermediate-scale flux ropes originate from solar eruptions, similar to MCs, since they had similar characteristics, such as the similar trend in annual number, low speed solar wind conditions under which they occurred, and similar axial orientation distributions. Cartwright et al. [72] did a comprehensive survey of small-scale flux ropes located between 0.3 and 5.5 AU heliocentric distances. They found that the occurrence of small-scale flux ropes had a solar cycle dependency, which implies that they may originate from the Sun. However, they also found that the lack of depressed proton

temperature and the location being near the sector boundary crossings implied that they may be created locally due to magnetic reconnection across the heliospheric current sheet. Feng et al. [73] examined the counterstreaming suprathermal electron (CSE) signatures of 106 small-scale flux ropes measured by Wind from 1995-2005. They found that the CSE appeared in most small-scale flux ropes located far from the heliospheric current sheets, while the CSE appeared in only half of the small-scale flux ropes located near the heliospheric current sheets. A limited number of studies also looked at the corresponding elemental composition and charge state signatures within small-scale flux rope intervals [73]. By using hourly data, those authors found from a subset of small-scale flux rope events identified between 1995 and 2007 that these structures share some common features with MCs. They provided supporting evidence for the origin of small-scale flux ropes from solar corona, although for a very limited number of events of durations usually lasting about a few hours.

Small scale magnetic flux ropes are considered to be associated with particle energization. Simulation results suggested that the interaction of multiple magnetic islands is intrinsic in reconnection process and related to particle energization [74–77]. When some electrons which are pre-energized during reconnection and island formation are injected into magnetic islands (strictly 2-D flux ropes), they will continue to gain energy within the island due to a classic Fermi acceleration process [74]. Zank et al. [78] derived a gyrophase-averaged transport equation to describe the pitch-angle scattering and energization of particles in quasi-2-D magnetic islands interaction process, in which the charged particles trapped in magnetic islands are scattered and energized via interactions with the induced electric field and contracting magnetic

islands. le Roux et al. [79] suggested that reconnection electric fields from merging flux ropes can cause ion drift acceleration, which accelerates suprathermal ions to power-law spectra. Using transport theory, Zank et al. [80, 81] investigated the combined effect of diffusive shock acceleration (DSA) and multiple magnetic island charged-particle acceleration mechanism downstream of a shock. They found that both the merging plasmoid reconnection-induced electric field and downstream plasmoid contraction can cause a power law particle speed spectrum, which is flatter than that derived from the conventional DSA theory alone. Figure 1.4 is a schematic proposed by Zank et al. [81]. The charged particles diffuse spatially by Alfvénic-like fluctuations via pitch-angle scattering, then these particles are trapped and energized by island contraction and repeatedly encountering with the anti-reconnection electric field.

Accumulating observational evidence supports the theory of particle acceleration in multiple magnetic islands. Khabarova et al. [82] showed the cases of particle acceleration associated with merging magnetic islands near the reconnecting HCS, and particle acceleration in magnetic islands confined near an ICME and the HCS. These structures were associated with enhanced energetic particle flux in absence of other sources. In a follow-up paper, Khabarova et al. [83] provided more evidence showing that the pre-accelerated particles (up to keV) can be further accelerated up to 1~1.5 MeV inside the regions where magnetic islands are confined and contractions may occur due to the increasing pressure. Khabarova and Zank [84] presented case studies showing that an atypical energetic particle event (AEPE) encompassed the reconnection exhaust. They suggested that the small-scale magnetic islands trapped

the energetic particles and accelerated them up to  $\sim 5$  MeV after these particles were pre-accelerated by prolonged magnetic reconnection.

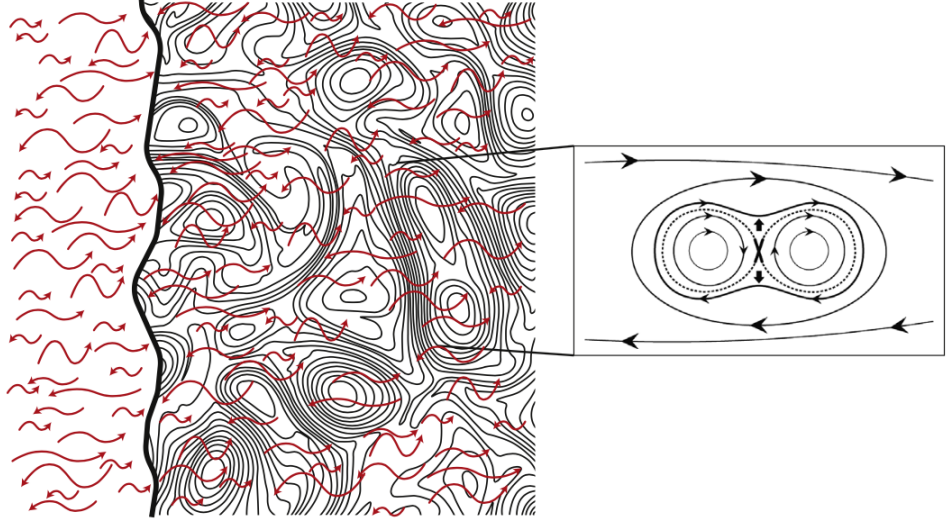


**Figure 1.4:** Schematic of merging magnetic islands (plasmoids or flux ropes in strictly 2-D) downstream of a shock proposed by Zank et al. [81]. The heavy black wavy line represents a shock. The red wavy lines are Alfvénic-like fluctuations. The right panel illustrates the magnetic reconnection associated with a pair of merging magnetic islands.

The geoeffectiveness of small-scale flux ropes also attracted researchers' interest. It is widely accepted that the MCs are one type of the major drivers of geomagnetic activities, such as the geomagnetic storms. Since the magnetic clouds and small-scale magnetic flux ropes have the similar magnetic field configuration but distinct scale sizes, researchers believe that the small magnetic flux ropes are capable of triggering some corresponding geomagnetic activities, but perhaps in a different manner. More and more studies suggested that the small scale flux ropes are closely related to substorms. Feng et al. [85] examined 26 small scale magnetic flux ropes observed by Wind spacecraft during 2000 to 2002, and found that 18 of them were

associated with substorms. Zhang et al. [86] identified 16 small-scale magnetic flux ropes observed by Wind and ACE during 2007 to 2008, and found 13 of them were associated with substorm activity. However, studies on the geoeffectiveness of small-scale flux ropes are still limited and the result is not conclusive.

### 1.3 Research Objectives

To recap, as one type of the important coherent structures in heliosphere, small-scale magnetic flux ropes play an important role in space plasma processes. However, our understanding of the structure is still limited. Their formation mechanism and origination are still under debate, and the hypotheses of evolution and propagation process are based on insufficient database [69–73]. In contrast to their large-scale counterparts in the solar wind as direct consequences of energetic solar eruptions, these small to medium sized flux ropes are much less studied. The trend of their occurrence and properties varying with solar cycles as revealed from some previous analysis has yet to be firmly established.

Lately, research interest in these structures and related processes has gained significant momentum [74, 82–84, 87–96]. It has been shown that these structures play critical roles in energizing suprathermal particles, an important component of the particle population in the solar wind [74–79], and can act with shocks to further accelerate particles [80, 81]. They can also contribute to the presence of intermittent structures in the solar wind, an intrinsic ingredient in solar wind turbulence [89, 97–103]. Such intermittency, fundamental to the dynamic processes in solar wind plasmas, can be naturally explained by the presence of these flux rope (or “flux

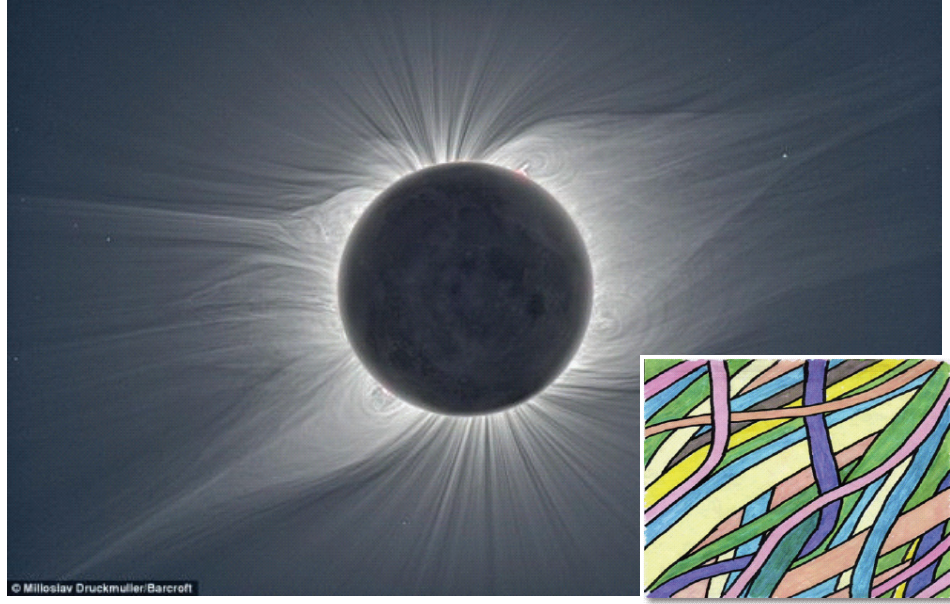


**Figure 1.5:** The structured solar corona during a total eclipse (Credit: Miloslav Druckmüller, Peter Aniol, Martin Dietzel, Vojtech Rusin). The bright streamline-like features represent plasma and magnetic structures. The inset depicts artistically one hypothetical scenario of “flux ropes” permeating the interplanetary space, originating from those filamentary structures near the Sun (Inset credit: Borovsky et al. [104]; see also Bruno et al. [106]).

tube”) structures, as depicted in Figure 1.5, where the crossing of the flux ropes and their boundaries leads to discrete and abrupt changes in magnetic field and plasma properties, as manifested in time-series data [104]. However such a hypothesis has yet to be verified. In addition, theoretical investigations [78, 80, 81, 93, 103, 105] envisaged the indispensable role of the existence of and interaction among these structures, responsible for trapping and energization of charged particles in space. Therefore it is of significant intellectual merit to quantitatively examine these structures, to elucidate their configuration and to establish their correspondence to closely related processes, from direct spacecraft measurements.

Therefore, our research objectives are (1) to build a comprehensive small-scale magnetic flux rope database via extensive events searching, which is to be used in this dissertation and made public for a wider user community, (2) to uncover the intuitive perception of small-scale magnetic flux rope appearance in the solar wind, examining the “flux rope sea” or the “sea (archipelago) of magnetic islands” [84] hypothesis, (3) to investigate their formation mechanism(s), origination, and association with other transients and structures in the heliosphere by statistical analysis based on our newly developed database, and (4) to provide observational evidence for the particle acceleration theories associated with small-scale magnetic flux ropes by a series of case studies.

#### 1.4 Research Methodology

The primary goal of our research is to build a comprehensive database covering a long time period. The main challenge we encounter is to find a reliable method to identify small-scale magnetic flux ropes. Most of the previous studies employ an axisymmetric, constant-alpha, linear force-free magnetic field model to fit the one-dimensional spacecraft data across a magnetic flux rope [107, 108]. A simple solution of such a model was found by Lundquist [109], in which the axial and transverse field components are proportional to the zeroth and first-order Bessel functions of the first kind, respectively. Other similar 1-D models also exist. However, these models are mostly limited to a pre-defined 1-D cross-section geometry and force-free condition. In reality, most of the small-scale magnetic flux ropes are not in the perfect cylindrically

symmetric shape in general. These models also omit plasma pressure gradient within the flux ropes, which is not consistent with observations.

Alternatively, Hu and Sonnerup [110, 111] applied the Grad-Shafranov (GS) reconstruction technique to the in-situ data collected when the spacecraft crosses the flux rope structure. The GS method is a true two-dimensional (2-D) method that can derive a 2-D cross section of magnetic and plasma configurations in space from 1-D spacecraft data. It has been developed and applied for a number of years [26, 110–122]. In the GS reconstruction, axisymmetry and the force-free assumption are abandoned. Some reconstruction results showed the obvious distortion from the axisymmetric geometry. The multiple, nonsymmetric flux rope structures of mesoscales in the solar wind were reconstructed by Hu et al. [115] using the GS reconstruction technique. These structures had the double or triple flux rope configurations, in which one flux rope is located immediately next to the other. The magnetic X line between adjacent flux ropes implied that they may be relics of end product of a dynamic evolution process due to magnetic field reconnection during or after an active merging process.

The advantage of the GS model over previous models is that it is able to recover the nonsymmetric geometry of the small-scale flux ropes in a more general non-force-free configuration, and the reconstruction algorithm can be automated for batch-mode executions on large datasets. It also has limitations. For example, the quasi-static equilibrium assumption restricts its application to structures without significant remaining plasma flows in their proper frames of reference. To overcome this limitation, Sonnerup et al. [123] have developed a basic approach for 2-D time-stationary, ideal, compressible, coherent MHD reconstruction technique that can account for signifi-

cant remaining plasma flow within the structure. This improvement has yet to be implemented in the small-scale flux rope reconstructions to account for the additional event candidates with the magnetic field and significant plasma flow configurations in dynamic equilibrium with additional inertial force.

In this dissertation, we adopt the quasi-static GS equation to describe the magnetic flux rope configuration, and develop an automated detecting algorithm to scan in-situ spacecraft measurements over two solar cycles to look for flux rope structures. The data used in the flux rope detecting process include time-series magnetic field vectors, and plasma bulk properties such as flow velocity, plasma temperature and density, including both protons and electrons when available. To guarantee the quality of the flux rope database, we set a series of criteria/metrics to rule out the non-flux-rope structures which may survive in the flux rope searching process. For example, to exclude Alfvénic structures, we apply the Walén test to each flux rope candidate, and remove the records with Walén slopes of significant magnitudes. Since the average magnetic field magnitude in the solar wind is about 5 nT, we remove the records with average magnetic field less than 5 nT. For a detailed description of the detection procedure, see Chapter 3.

Until now, we have built a small-scale magnetic flux rope database based on the observational data with 1-minute cadence from Wind spacecraft. In the following chapters, we will present our newly developed database and carry out a statistical analysis as well as case studies based on the database. We also publish the database online and make it available to the public, via <http://fluxrope.info>.

## 1.5 Organization of This Dissertation

The dissertation is organized as follows. Chapter 1 provides some background information on transients and structures in the solar wind, emphasizing the space environment in which small-scale magnetic flux ropes occur. We also provide a literature review on the current research progress on small-scale magnetic flux ropes. Chapter 2 elaborates on the theory of Grad-Shafranov (GS) equation and the GS reconstruction technique. The detailed derivation of the GS equation will be presented in this chapter. Chapter 3 describes the development of the automated small-scale magnetic flux rope detection algorithm. We will elaborate on the technical details on how to develop the flux rope detection algorithm based on the Grad-Shafranov reconstruction technique. The entire procedure of building the flux rope database will also be presented. Chapter 4 presents the small-scale magnetic flux rope database built by our new algorithm. Then we will carry out a statistical analysis on the events from our database and summarize some essential findings. We will discuss the implication for the origination and formation mechanism of small-scale magnetic flux ropes, and their relation to solar activity and other transients and structures in the heliosphere. The “sea of flux rope” hypothesis will be examined using the new database. In Chapter 5, we show the case studies on particle acceleration associated with small-scale magnetic flux ropes, and discuss the correspondence between theoretical predictions and observational results. Chapter 6 concludes this dissertation and offers an outlook for future work to be performed, using the small-scale magnetic flux rope database.

## CHAPTER 2

### GRAD-SHAFRANOV RECONSTRUCTION TECHNIQUE

#### 2.1 Introduction

The Grad-Shafranov (GS) reconstruction technique is a tool to recover two-dimensional (2-D) magnetohydrostatic structures from one-dimensional (1-D) in-situ spacecraft data. With this technique, a 2-D coherent magnetic field structure, e.g., the cross section of a magnetic flux rope, can be reconstructed from 1-D time series data collected as such a structure passes observing instruments on board a spacecraft. The Grad-Shafranov reconstruction technique was first developed and applied to a magnetopause crossing of the tangential-discontinuity type by Sonnerup and Guo [112]. This technique was further developed by Hu and Sonnerup [110, 111] to be applied to magnetic flux ropes. The advantage of this technique is that it adopts a more general non-force-free assumption, and does not presume the cross section to be of axisymmetry or other regular geometry. Since this technique is able to find more types of flux ropes, no matter whether they are force-free, non-force-free, axisymmetric or nonaxisymmetric, we expect to detect more events by using this method in order to build a more comprehensive database of small-scale magnetic flux ropes.

In a review article by Sonnerup et al. [117], the theoretical background of the GS reconstruction was described in detail. Hu and Sonnerup [111] also elaborated the technical details for applying this technique to magnetic flux ropes. For a most recent comprehensive review on the GS reconstruction technique, see Hu's paper [26], commemorating the twentieth anniversary of the advent of the technique. Here we summarize the theory and the relevant procedures of GS reconstruction, from the perspective of its application to detect small-scale magnetic flux ropes.

## 2.2 Two-dimensional Magnetohydrostatic Equilibrium

Starting with the single-fluid MHD equation,

$$\rho \frac{\partial \mathbf{v}}{\partial t} + \rho \mathbf{v} \cdot \nabla \mathbf{v} = \mathbf{j} \times \mathbf{B} - \nabla p + \rho \mathbf{g}, \quad (2.1)$$

ignoring the gravitational force and the inertial force, i.e., in a magnetohydrostatic equilibrium and a proper frame of reference, we have  $\mathbf{g} = 0$ ,  $\mathbf{v} \equiv 0$ , and  $\frac{\partial}{\partial t} = 0$ . Equation (2.1) becomes

$$\nabla p = \mathbf{j} \times \mathbf{B}. \quad (2.2)$$

Equation (2.2) describes the force balance, for example, in a magnetic flux rope. The magnetic field in the magnetic flux rope also satisfies the Ampère's law

$$\nabla \times \mathbf{B} = \mu_0 \mathbf{j}, \quad (2.3)$$

and the divergence free condition

$$\nabla \cdot \mathbf{B} = 0. \quad (2.4)$$

Additionally, considering that in a cylindrical flux rope, the variation along the axial direction is much more gradual than that in the transverse direction. We can assume that the magnetic field and plasma equilibrium has the translation symmetry along the axial direction. Without loss of generality, we can lay the flux rope axis along the  $z$ -axis in a Cartesian coordinate system. So the transverse plane coincides with the  $x$ - $y$  plane. With translational symmetry assumption along the  $z$ -axis, we have the condition

$$\frac{\partial}{\partial z} = 0. \quad (2.5)$$

Equations (2.2), (2.3), (2.4) and condition (2.5) define a magnetic flux rope configuration with cylindrical geometry and translational symmetry along the  $z$ -axis in the Cartesian coordinates, but with arbitrary cross-sectional shape and generally non-vanishing axial magnetic field,  $B_z$ .

### 2.3 Field Line Invariants

Equation (2.2) shows that the gradient of plasma pressure  $p$  is perpendicular to  $\mathbf{j}$  and  $\mathbf{B}$ , so  $p$  itself must be constant along  $\mathbf{B}$  field line. The plasma pressure  $p$  becomes a field line invariant. Making use of the magnetic vector potential, the magnetic field  $\mathbf{B}$  can be represented as  $\mathbf{B} = \nabla \times \mathbf{A}$ . Expand it and make use of condition (2.5), then

we have  $B_x = (\partial A_z / \partial y)$ ,  $B_y = -(\partial A_z / \partial x)$ , and  $B_z = (\partial A_y / \partial x - \partial A_x / \partial y)$ . In the transverse plane, we re-write  $A_z = A(x, y)$ . Then the magnetic field can be expressed as

$$\mathbf{B} = \left[ \frac{\partial A(x, y)}{\partial y}, -\frac{\partial A(x, y)}{\partial x}, B_z \right]. \quad (2.6)$$

The variable  $A$  is also the magnetic flux function, since the difference in  $A$  values yields the poloidal magnetic flux per unit length enclosed within the flux surfaces characterized by distinct  $A$  values.

Similarly by expanding Equation (2.2) and making use of condition (2.5), we get  $j_x B_y - j_y B_x = 0$ , i.e.,  $B_y / B_x = j_y / j_x$ . Since in the transverse plane, the field line equation of  $\mathbf{B}$  is  $B_y / B_x = dy / dx$ , we have

$$\frac{B_y}{B_x} = \frac{j_y}{j_x} = \frac{dy}{dx}. \quad (2.7)$$

In Equation (2.7) , replacing  $B_x$  and  $B_y$  with their vector potential representations from Expression (2.6) , we have

$$\frac{\partial A(x, y)}{\partial x} dx + \frac{\partial A(x, y)}{\partial y} dy = 0. \quad (2.8)$$

Similarly, we get

$$dA(x, y) = 0, \text{ along magnetic field lines.} \quad (2.9)$$

Equation (2.9) shows that  $A(x, y)$  is a field line invariant.

Equation (2.7) shows that in the  $x$ - $y$  plane, the current density is parallel and proportional to the transverse magnetic field. Denoting the transverse component of the current density as  $\mathbf{j}_t$ , then  $\mathbf{j}_t$  is also a field line invariant.

Similarly from Equation (2.3) and condition (2.5), we obtain  $\mu_0 j_x = \partial B_z / \partial y$ ,  $\mu_0 j_y = -\partial B_z / \partial x$ , and  $\mu_0 j_z = \partial B_y / \partial x - \partial B_x / \partial y$ . With the first two equations, we have

$$\frac{j_x}{j_y} = \frac{\partial B_z / \partial y}{-\partial B_z / \partial x}. \quad (2.10)$$

From Equations (2.7) and (2.10), we get

$$\frac{\partial B_z}{\partial x} dx + \frac{\partial B_z}{\partial y} dy = \nabla B_z \cdot d\mathbf{r} = 0. \quad (2.11)$$

In the  $x$ - $y$  plane,  $B_z$  is the function of  $x$  and  $y$ . So the left-hand side of Equation (2.11) is the total differential of  $B_z$ . Therefore,

$$dB_z(x, y) = 0, \text{ along magnetic field lines.} \quad (2.12)$$

This indicates that  $B_z$  is also a field line invariant and is a function of  $A$ .

Until now, we have obtained four field line invariants, the plasma pressure  $p$ , the transverse current density  $j_t$ , the axial component of the magnetic field  $B_z$ , and the axial component of the vector potential  $A(x, y)$ . With these four field line invariants, we are able to derive the Grad-Shafranov equation.

## 2.4 The Grad-Shafranov Equation

Since both  $A(x, y)$  and  $B_z$  are field line invariants,  $B_z$  must be a single variable function of  $A$ . We can further rewrite Expression (2.6) as

$$\mathbf{B} = \left[ \frac{\partial A(x, y)}{\partial y}, -\frac{\partial A(x, y)}{\partial x}, B_z(A) \right] = \nabla A \times \hat{\mathbf{z}} + B_z \hat{\mathbf{z}}. \quad (2.13)$$

So the transverse component of  $\mathbf{B}$  is

$$\mathbf{B}_t = \nabla A \times \hat{\mathbf{z}}. \quad (2.14)$$

Using  $\hat{\mathbf{z}}$  to cross multiply both sides of Equation (2.14), we have

$$\hat{\mathbf{z}} \times \mathbf{B}_t = \nabla A. \quad (2.15)$$

The transverse component of Equation (2.3) is

$$\mathbf{j}_t = \frac{1}{\mu_0} (\nabla \times \mathbf{B})_t = \frac{1}{\mu_0} \left[ \left( \frac{\partial B_z}{\partial y} - \frac{\partial B_y}{\partial z} \right) \hat{\mathbf{x}} + \left( \frac{\partial B_x}{\partial z} - \frac{\partial B_z}{\partial x} \right) \hat{\mathbf{y}} \right], \quad (2.16)$$

and with the translational symmetry condition  $\partial/\partial z = 0$ , we have

$$\mathbf{j}_t = \frac{1}{\mu_0} \left( \frac{\partial B_z}{\partial y} \hat{\mathbf{x}} - \frac{\partial B_y}{\partial x} \hat{\mathbf{y}} \right) = \frac{1}{\mu_0} \nabla B_z \times \hat{\mathbf{z}}. \quad (2.17)$$

The  $z$  component of Equation (2.3) is

$$j_z \hat{\mathbf{z}} = \frac{1}{\mu_0} (\nabla \times \mathbf{B})_z = \frac{1}{\mu_0} \left( \frac{\partial B_y}{\partial x} - \frac{\partial B_x}{\partial y} \right) \hat{\mathbf{z}}. \quad (2.18)$$

Make use of the vector potential of  $\mathbf{B}$ , then we get

$$j_z = \frac{1}{\mu_0} \left( -\frac{\partial^2 A}{\partial x^2} - \frac{\partial^2 A}{\partial y^2} \right) = -\frac{1}{\mu_0} \nabla^2 A. \quad (2.19)$$

Decompose  $\mathbf{j}$  and  $\mathbf{B}$  in Equation (2.2) into the transverse and the axial components, then we can write it as (recall that  $\mathbf{j}_t \parallel \mathbf{B}_t$ )

$$\nabla p = (\mathbf{j}_t + j_z \hat{\mathbf{z}}) \times (\mathbf{B}_t + B_z \hat{\mathbf{z}}) = \mathbf{j}_t \times \hat{\mathbf{z}} B_z + j_z (\hat{\mathbf{z}} \times \mathbf{B}_t). \quad (2.20)$$

Substitute the term  $\hat{\mathbf{z}} \times \mathbf{B}_t$  and the variables  $\mathbf{j}_t$  and  $j_z$  in Equation (2.20) with their expressions in Equation (2.15), (2.17), and (2.19), respectively, then we have

$$\nabla p = -\frac{1}{\mu_0} B_z \nabla B_z - \frac{1}{\mu_0} \nabla^2 A \nabla A. \quad (2.21)$$

Since both  $p$  and  $B_z$  are field line invariants, both of them are single variable functions of  $A$ . So we have

$$\nabla p = \frac{dp}{dA} \nabla A, \quad (2.22)$$

and

$$\nabla B_z = \frac{dB_z}{dA} \nabla A. \quad (2.23)$$

Substitute Equations (2.22) and (2.23) into Equation (2.21) and simplify the result, then we get

$$\nabla^2 A = -\mu_0 \frac{d(p + B_z^2/2\mu_0)}{dA}. \quad (2.24)$$

Define the total transverse pressure

$$P_t = p + \frac{B_z^2}{2\mu_0}, \quad (2.25)$$

and substitute it into Equation (2.24), then we get

$$\nabla^2 A = -\mu_0 \frac{dP_t}{dA}. \quad (2.26)$$

From Equations (2.19) and (2.26), we note that the total derivative  $dP_t/dA$  is just the axial current density  $j_z$ . Therefore Equation (2.26) can be written in a more common form,

$$\frac{\partial^2 A}{\partial x^2} + \frac{\partial^2 A}{\partial y^2} = -\mu_0 \frac{dP_t}{dA} = -\mu_0 j_z(A). \quad (2.27)$$

Equation (2.27) is the standard Grad-Shafranov (GS) equation. The GS equation describes non-force-free, magnetohydrostatic magnetic field structure. In this study, it describes the cross section of a magnetic flux rope. Solving this equation numerically [113], we can reconstruct the 2-D structure of a magnetic flux rope. Note that the quantity  $P_t$  is a single variable function of  $A$ . This is an important property that we are going to use in the automated magnetic flux rope detection algorithm to be described in Chapter 3.

## 2.5 GS Reconstruction Examples

In this section, we describe the GS reconstruction technique briefly, and show three reconstruction examples. To reconstruct the cross section of a magnetic flux rope, we need to compute two quantities, the thermal pressure  $p$ , and the magnetic flux function  $A$ , from the observational data along the spacecraft path. In Equation (2.25), the thermal pressure  $p$  can be calculated from the plasma number density ( $N_e = N_p = N$ ) and temperature (proton temperature  $T_p$ , and electron temperature  $T_e$ ),

$$p = Nk(T_e + T_p). \quad (2.28)$$

The magnetic flux function  $A$  can be calculated from the magnetic field measurements and the deHoffmann-Teller (HT) frame velocity [111],

$$A(x, 0) = \int_0^x \frac{\partial A}{\partial \xi} d\xi = \int_0^x -B_y(\xi, 0) d\xi, \quad (2.29)$$

where  $d\xi = -\mathbf{V}_{HT} \cdot \hat{\mathbf{x}} dt$ . The  $\mathbf{V}_{HT}$  is the constant HT frame velocity,  $\hat{\mathbf{x}}$  is the unit vector of the  $x$ -axis of the reconstruction frame along the spacecraft path, and  $dt$  is the sampling time interval.

In practice, we follow the basic reconstruction steps described in the paper by Hu and Sonnerup [111]. The first step is to find a co-moving frame of reference, which is usually the deHoffmann-Teller (HT) frame [124–126]. This is achieved by minimizing the residual electric field of a frame moving with a yet-to-be-determined velocity. In the ideal case, the residual electric field can be transformed to zero in

the HT frame. Then the minimum-variance analysis is applied to find three eigenvalues (the minimum, intermediate, and maximum covariances) and the corresponding eigenvectors. We take the direction along the intermediate eigenvector as the initial trial  $z$ -axis. A trial-and-error process is carried out to find the optimal  $z$ -axis orientation first, based on the requirement of  $P_t(x, 0)$  *versus*  $A(x, 0)$  being single-valued. The spacecraft data are projected onto the local reconstruction coordinates  $(x, y, z)$ , in which the spacecraft path is along the positive  $x$ -axis direction, and the  $y$ -axis completes the right-handed orthogonal coordinate system. Next we integrate the measured  $B_y(x, 0)$  to obtain the value  $A(x, 0)$  through Equation (2.29). Once the  $z$ -axis is determined by fitting the data pairs  $P_t(x, 0)$  *versus*  $A(x, 0)$ , we obtain an analytic function for the transverse pressure  $P_t(A)$ . Using the known function  $P_t(A)$  and initial values given by the spacecraft measurements along  $y = 0$ , we solve the GS equation [113] to obtain the solution of the flux function  $A(x, y)$  in a rectangular domain on the cross section perpendicular to  $z$ , which fully characterizes the  $2\frac{1}{2}$ -D magnetic field configuration of the flux rope.

We present three examples of the GS reconstruction as applied to small-scale flux ropes in an earlier study [94]. Figure 2.1 shows three small-scale flux rope intervals that were identified behind an interplanetary shock. The shock interface was observed on 2002 Jan. 31, 21:38 UT. It is denoted by a vertical dashed line. We can see that the magnetic field magnitude jumps at the shock interface. All magnetic field components changed accordingly. Three small-scale flux rope intervals were marked based on mainly magnetic field measurements and the GS reconstruction results to be presented. The magnetic field magnitude kept at a high level (about 12 nT) down-

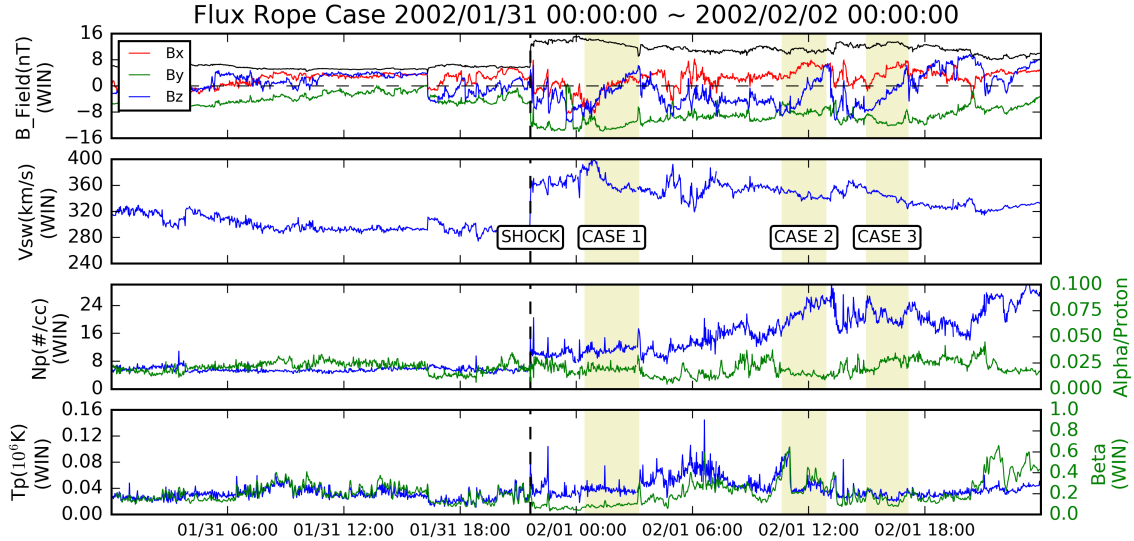


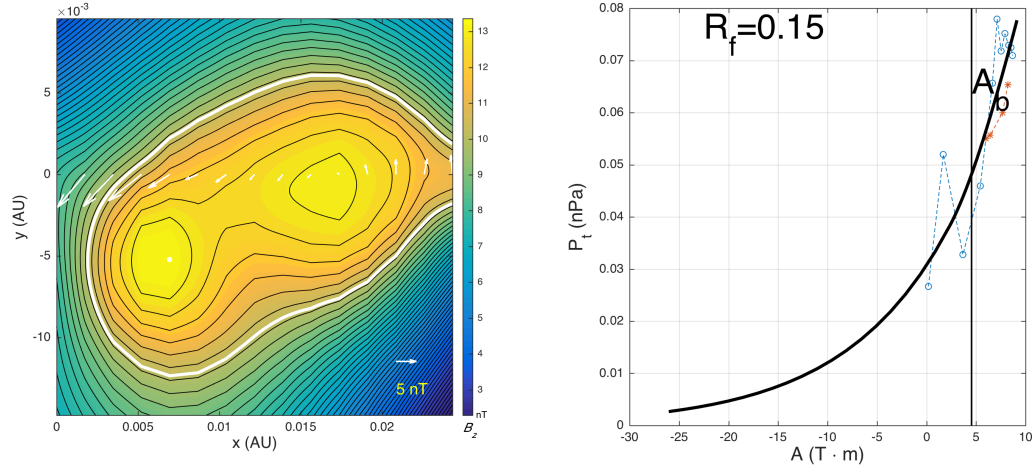
**Figure 2.1:** Time series data from 2002 Jan. 31, 00:00 UT to 2002 Feb. 2, 00:00 UT. This time interval contains one interplanetary shock and three flux rope structures. The first panel is the magnetic field data from Wind. The black solid line denotes the total magnetic field magnitude. The second panel is the solar wind bulk speed from Wind. In the third panel, the proton number density is shown in blue line and the alpha/proton ratio is shown in green line. These two sets of data are from Wind. The fourth panel are the proton temperature (in blue line) and plasma beta (in green line), both of which are from Wind. The proton temperature (in  $10^6$  K) was calculated from proton thermal speed, and the plasma beta was calculated from proton number density, proton temperature, and the magnetic field. The contribution of electrons to plasma beta was not taken into account, because there was no electron temperature data available. The shock is denoted by a vertical black dashed line. The time of this shock is 2002 Jan. 31, 21:38 UT. The shaded regions represent three small scale flux ropes, which are labeled as CASE 1, CASE 2 and CASE 3, respectively.

stream of the shock, together with elevated solar wind flow speed. The second panel shows that the solar wind speed was enhanced from about 280 km/s to about 360 km/s downstream across the shock interface. These were not typically high speed. The third panel shows that the proton density (in blue color) and the alpha/proton number density ratio changed drastically in the downstream of the shock. It is generally believed that higher alpha/proton ratio implies a coronal source of the plasma.

In the last panel, we can see that the proton temperature increased in CASE 1 and CASE 2. In CASE 3, the proton temperature decreased but was still above that in ambient solar wind. This temperature characteristic is different from that of a magnetic cloud, in which the proton temperature is depressed. The average plasma beta values during the time intervals of CASE 1 and CASE 3 were 0.09 and 0.14, respectively. These values were close to the typical plasma beta value in MCs ( $\lesssim 0.1$ ). The average plasma beta value during the time interval of CASE 2 was 0.33, which was above that of MCs.

### 2.5.1 CASE 1: Wind 2002/2/1 00:25 ~ 03:15 UT

The GS reconstruction result of CASE 1 is shown in Figure 2.2(a). We can see a twin flux rope structure from Figure 2.2(a). This kind of structure was reconstructed and studied earlier by Hu et al. [115]. The core fields of these two adjacent flux ropes are about 13 nT. The time duration of the entire event was 2 hours and 50 minutes. The flux rope on the left had a scale size of about 0.0075 AU, and the right one had a scale size of about 0.01 AU. From the white arrows we can see that both of them had right-handed chirality. An  $X$  point geometry may be formed by magnetic reconnection between the two flux ropes. Figure 2.2(b) is the fitting curve of  $P_t(A)$ , which is the transverse plasma pressure, the sum of plasma and the axial magnetic pressure. According to the GS reconstruction theory,  $P_t(A)$  must be a single value function of the magnetic flux function  $A$ . The value  $R_f$  in the graph is the fitting residue. It is the normalized deviation of the measured data points from the fitted

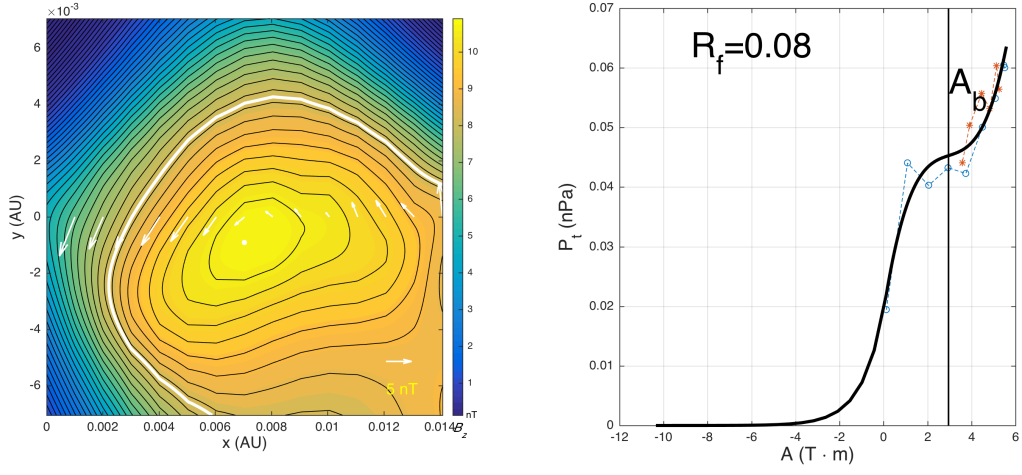


(a)  $\hat{\mathbf{z}} = [0.14, -0.99, -0.0089]$

(b)

**Figure 2.2:** GS reconstruction result for CASE 1 (2002 Feb. 1, 00:25 - 03:15 UT). (a) The cross-section magnetic field configuration of the flux rope. The unit vector  $\hat{\mathbf{z}}$  represents the  $z$ -axis orientation of the flux rope in GSE coordinates. The filled color contour represents the axial magnetic field  $B_z$  and the line contour overlapped in black represents the transverse magnetic field lines. The white dot in the center is the location of the maximum axial field  $B_z$ . The white arrows across the map horizontally are projected transverse magnetic field vectors along the spacecraft path. The white contour line encloses the region  $A > A_b$ , denoted in (b). The reconstruction map within this line is reconstructed by double-folded  $P_t(A)$  data, and the region beyond this line is reconstructed based on the extrapolated data. (b) The fitting curve (bold solid line) of  $P_t(A)$  for CASE 1. The fitting is based on the data points marked by blue circles and red stars, where the circles represent the data as spacecraft was crossing the first half of the flux rope structure and the stars represent those of the second half. The thin vertical solid line denoted by  $A_b$  marks the boundary corresponding to the white contour line in Figure 2.2(a).

curve, which was defined in the paper by Hu et al. [115]. In this case, the residue is 0.15. We consider the fitting with a residue below 0.3 as an acceptable result.



(a)  $\hat{\mathbf{z}} = [0.73, -0.67, -0.10]$

(b)

**Figure 2.3:** GS reconstruction result for CASE 2 (2002 Feb. 1, 10:36 - 12:55 UT). The format is the same as in Figure 2.2.

### 2.5.2 CASE 2: Wind 2002/2/1 10:36 ~ 12:55 UT

The reconstruction result of CASE 2 is shown in Figure 2.3. The time duration was 2 hours and 19 minutes, and the scale size was about 0.01 AU. The core field of this flux rope was about 11 nT. The chirality was right-handed, which was the same as that in CASE 1. This reconstruction has a fitting residue of 0.08 (see Figure 2.3 (b)), which is a very small value, indicating a trustworthy reconstruction. From the third panel of Figure 2.1, we can see that the proton number density was much higher than that of CASE 1. But the alpha/proton ratio was similar to that of CASE 1, indicating number density enhancements in both protons and alpha particles. The proton temperature was enhanced at the beginning of CASE 2, then dropped to the same level as that of CASE 1.

### 2.5.3 CASE 3: Wind 2002/2/1 14:57 ~ 17:03 UT

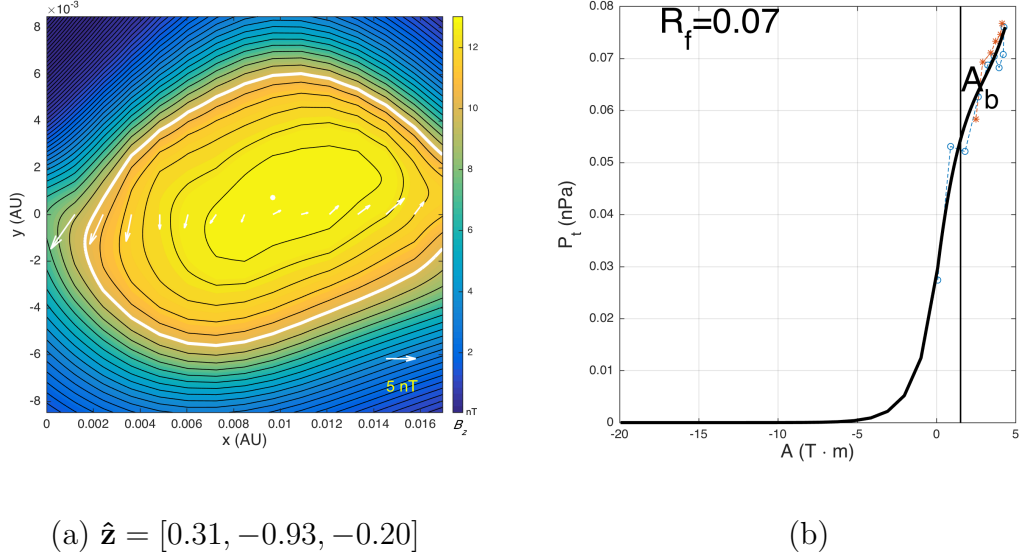


**Figure 2.4:** GS reconstruction result for CASE 3 (2002 Feb. 1, 14:57 - 17:03 UT). The format is the same as in Figure 2.2.

The reconstruction result of CASE 3 is shown in Figure 2.4. Figure 2.4 (b) shows the fitting curve of function  $P_t(A)$  with a small fitting residue 0.07. From Figure 2.4 (a) we can see that the spacecraft crossed the cross section of this flux rope near the central axis. The duration of this flux rope was 2 hours and 6 minutes, and its scale size was about 0.015 AU. It had the same right-handed chirality as that of CASE 1 and CASE 2. Figure 2.1 shows that CASE 3 also had the high proton number density and temperature. The average plasma beta value was 0.14, which was close to the typical value, 0.1, in MCs.

From the three cases shown above, we find that multiple small-scale flux ropes exist downstream of a shock. None of them showed the depressed proton temperature.

Two cases (CASE 1 and CASE 3) had similar plasma beta values to that of MCs, and one case (CASE 2) had higher plasma beta value than that of MCs. A Halo CME occurred at 2002 Jan. 27, 12:30:05 UT, which was a possible source to drive the shock. Given the plasma profiles different from typical MCs, these small-scale flux ropes may not be generated on the Sun by the CME. They may be produced by the shock, or some other processes in the inner heliosphere. The same chirality of the three flux ropes may hint at the same process or the same environment in which they were generated.

## CHAPTER 3

### AUTOMATED DETECTION ALGORITHM BASED ON THE GS METHOD

To apply the automated detection algorithm based on the GS method, the first problem to be resolved is to find an appropriate frame of reference in which the flux rope will be reconstructed. Due to the magnetohydrostatic assumption in the GS based model, the magnetic field structure to be examined by this model should be stationary. In other words, the magnetic field in such a structure has to be time-independent. Since the magnetic flux ropes embedded in ambient solar wind have significant bulk flows viewed in the *GSE* frame, we have to find an appropriate frame of reference in which the magnetic structure appears approximately stationary in order to apply the GS based algorithm. The deHoffmann-Teller (HT) frame is usually adopted as such a quasi-stationary frame. The deHoffmann-Teller (HT) frame [124] is a Galilean frame of reference in which all three components of the electric field vanish. In such a frame, since  $\mathbf{E}' = 0$ , with Faraday's law, we have  $-\partial\mathbf{B}'/\partial t = \nabla \times \mathbf{E}' = 0$ , i.e.,  $\mathbf{B}'$  is time independent. Note that the  $\mathbf{E}' = 0$  is a stronger restriction than  $\nabla \times \mathbf{E}' = 0$ . Generally an HT frame can be always found from the in-situ solar wind measurements, and the quality of which can be judged by a number of specific

metrics. Denoting the velocity of HT frame with respect to the *GSE* frame as  $\mathbf{V}_{HT}$ , once  $\mathbf{V}_{HT}$  is found, all the measured quantities can be easily transformed to the HT frame.

The second problem to be resolved is to determine the magnetic flux rope axial orientation. To reconstruct a cylindrical flux rope, all the quantities should be calculated in the flux rope frame,  $(x, y, z)$ , in which the  $z$ -axis is parallel to the flux rope axis, and the flux rope cross section is on the  $x$ - $y$  plane. However, in the flux rope detecting process, we do not know the flux rope orientation in advance. To determine the flux rope axial orientation, a popular but outdated method was to use the minimum variance analysis of magnetic field vector data (MVAB) [72, 127, 128]. Usually across the cross section of an axisymmetric flux rope, the measured in-situ time series magnetic field data will show the following profiles:  $B_x$  is small and nearly a constant,  $B_y$  varies from negative to positive (or vice versa), showing a bipolar profile, and  $B_z$  reaches its maximum magnitude in the center and decreases to the minimum magnitude at the two ends. As a result of such an idealized magnetic field configuration, the  $B_x$  component has the minimum variance, the  $B_y$  component has the maximum variance, and the  $B_z$  component has the intermediate variance. Therefore the MVAB analysis will generally yield the corresponding three principal axes with the eigenvector of the intermediate variance taken as the flux rope axial direction. However, this approach only works for well-defined flux rope profiles as mentioned above. Generally, a flux rope does not have axisymmetry, and in most cases, the flux ropes will be probably deformed by local plasma flow as they propagate outward from the sun. As a result, the variance analysis usually fails to yield the

optimal axial orientation. In practice, they only have limited use in providing a quick look of the desired pattern in the magnetic field rotation associated with the underlying flux rope configuration.

Hu and Sonnerup [2002] developed a new approach to determine the flux rope axial orientation base on the GS equation, specifically, the requirement that the function  $P_t$  *versus*  $A$  be single-valued and double-folded through a flux rope interval. In their approach, they define a fitting residue to evaluate how close the trial  $z$ -axis orientation is to the true  $z$ -axis orientation. If the trial  $z$ -axis deviates from the true axis, the two branches of  $P_t$  *versus*  $A$  will not be well folded, and the corresponding fitting residue will be larger than that of true  $z$ -axis orientation. In short, a trial-and-error process was devised to search for the optimal  $z$ -axis orientation in the whole space. An appropriately spaced search grid is constructed on the upper-half hemisphere of a unit sphere in a spherical coordinate, in which each grid point represents one trial  $z$ -axis orientation (represented by the polar angle  $\theta$  and the azimuthal angle  $\phi$ ). They traversed all grid points to find the  $z$ -axis orientation with minimum fitting residue of  $P_t(A)$ , which was taken as the optimal flux rope axial orientation. In our flux rope detection algorithm, we extend the usage of Hu and Sonnerup's approach. This approach is not only used for determining the optimal  $z$  axis of a flux rope, but also used for checking flux rope candidate. Since in the case of a cylindrical flux rope, an optimal  $z$ -axis with a reasonable small fitting residue will surely be found. Conversely, small fitting residue of  $P_t$  *versus*  $A$  is taken as a main criterion in identifying flux rope candidates, together with additional criteria to be presented in the following sections.

### 3.1 Automated Detection Algorithm

In the present study, we detect flux ropes with durations from about 10 minutes to 360 minutes. We split this task into multiple iterations. These iterations are: 10-15 minutes, 15-20 minutes, 20-25 minutes, ..., and 355-360 minutes. Each iteration identifies flux rope candidates with the durations falling in the time range specified. For example, when we run the 10-15 minutes iteration, we set a sliding window width to 15 minutes, and the lower limit of flux rope duration to 10 minutes. With this setting, the program checks the data segment in a 15-minute sliding window, and if the double-folded part of  $P_t(A)$  is less than 10 minutes, the program will discard it. When this iteration is done, the flux ropes with durations longer than 10 minutes and less than 15 minutes will be discovered and recorded. After all the given data is scanned by the 15-minute sliding window, we go to the next iteration to find flux ropes with other lengths. In practice, we extend the boundary of each iteration by 1 minute to make smooth conjunction between two adjacent iterations. Then the iterations become: 9-16 minutes, 14-21 minutes, 19-26 minutes, ..., and 354-361 minutes. We will explain later why we make this adjustment.

There are several reasons why we use the multiple iteration strategy. The first reason is that we need different smoothing levels to detect different length flux ropes. For example, a small fluctuation which is significant for a 10 minutes length flux rope may be negligible for a 60 minutes length flux rope. Moreover, because the long data segment tends to have more small fluctuations than short data segment, it is more likely to be rejected by the detection algorithm due to multiple turn points in  $P_t$ .

*versus A.* To guarantee both quality and quantity in the detecting process, we need to apply a strong smoothing process to make the long-duration flux ropes survive, while we need to apply a weak smoothing process to ensure that short flux ropes of bad quality are rejected. As to be explained, we use the third order Savitzky-Golay filter [129] to smooth the  $A$  array, and set the smoothing window width to be one half of the lower limit associated with each detection window width. The second reason to use a multiple window strategy is that we want to keep the coding logic and program architecture as simple as possible. If we try to use a large fixed-width sliding window to detect all sizes of flux ropes, we have to deal with many problems, especially when multiple flux rope structures exist in the window, such as trimming data segment, splitting multiple structures, moving window forward, so on and so forth. Furthermore, in the multiple flux rope structure, each individual flux rope may have different axial orientation, which makes fitting all of them in one window impossible. The code will be much simpler if we just seek for flux ropes with predefined duration or sizes in one iteration. The third reason is that we want to make the database easily expandable. If we decide to add flux ropes with additional durations to our database, what we need to do is to just run more iterations with new window widths, instead of repeating the entire process.

Therefore, the ground rules we play by are: (1) as many as possible flux rope candidates are to be identified by an exhaustive sifting process through the time-series data, and (2) a single flux rope is to be identified for each interval/event.

Now we are ready to introduce the flux rope detection algorithm. Our automated detection algorithm is based on the fact that the magnetic flux function  $A(x, y)$

is a field line invariant, and the transverse pressure  $P_t$  is a single-valued function of  $A$ , based on the GS method described in Chapter 2. As a spacecraft passes through the cross section of a magnetic flux rope with closed transverse field lines, it firstly crosses some transverse magnetic field lines in its first-half path toward the center, then it crosses exactly the same set of transverse field lines, but in reverse order, in its second-half path. Therefore, along the spacecraft path, the measured magnetic flux function  $A$  associated with the field lines traversed twice by the spacecraft shows a double-folded pattern, or contains a turn point (or inflection point) where an extremum is reached. Since the transverse pressure  $P_t$  is a single-valued function of  $A$ , the two branches of the data points along the first and second halves of the spacecraft path for  $P_t$  *versus*  $A$  should coincide as well. Conversely, given a specific time interval of interest, the transverse pressure  $P_t$  and the flux function  $A$  are calculated from the in-situ spacecraft data. Then we check whether the  $P_t$  *versus*  $A$  curve has the double-folded feature and how good the overlapping is. Later we will define the selection criteria. If the criteria are satisfied, the structure under checking is considered as a flux rope candidate.

A flowchart with control flow and data flow (Figure 3.1) is prepared to show the detailed technical procedures. The flowchart illustrates the flux rope detecting process with a fixed window width for one of the iterations described above. The inner loop is enclosed by the dashed lines, which shows the flux rope axial orientation determination process. The outer loop starting with the top rounded rectangle (“Set a detection window width”) shows the sliding window process, which moves the window forward to scan the entire time series data.

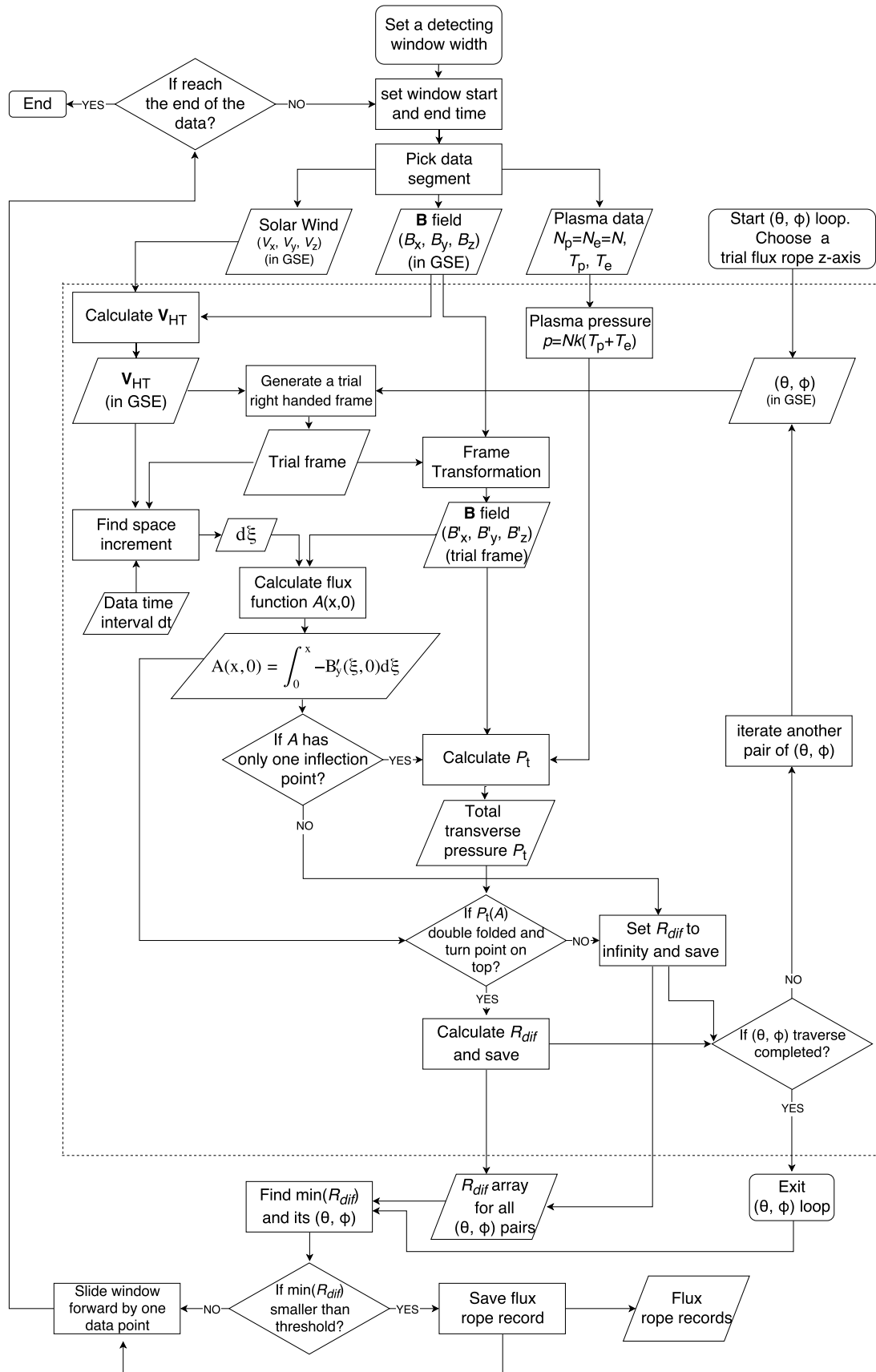


**Figure 3.1:** Flux rope detection algorithm flowchart. A rounded rectangle represents the beginning or end of a loop; a rectangle represents a process; a diamond represents a conditional judgement; and a parallelogram represents data input or output. The core loop is enclosed by the dashed lines.

A fixed width sliding window is used to select data. The window width defines the maximum duration of the flux rope to be detected during this iteration. We also define a lower limit of the flux rope duration. The flux ropes only with the durations between the lower and upper limits will be processed during this iteration. Later we are going to run multiple iterations with different window width to detect flux ropes with different sizes. Specifying the lower limit will avoid the duplication among the windows with different widths. For the time series magnetic field data within a given window, to make the  $P_t$  *versus*  $A$  curve double folded, the  $A$  array must have one and only one inflection point (or turn point), defined as the place where the magnetic field component  $B'_y$  changes sign (see Equation (3.1)). As discussed in Chapter 2, since the transverse pressure  $P_t$  is a single-valued function of  $A$ , the only way to make  $P_t$  *versus*  $A$  curve double folded is that the  $A$  array has to fold onto itself so that the  $P_t$  *versus*  $A$  curve has two branches. If the  $A$  array has more than one inflection point, the corresponding  $P_t$  *versus*  $A$  curve will be multiple folded, which does not meet the ground rule (2) for a single flux rope configuration. When such a situation occurs, the window may contain more than one flux rope structures. We just need to narrow down the window size to make it contain only one single flux rope structure. On the other hand, a narrow window cannot detect the flux ropes with the sizes longer than it. Therefore, to detect flux ropes with different sizes, we have adopted the strategy of running multiple windows with different widths.

In the detection program, the number of inflection points is examined by checking the number of extrema of  $A$  values in the window. The segments with more than one extreme  $A$  values, excluding the boundaries, will be discarded. In

practice, the local extrema in the  $A$  array may be caused by measurement error or small fluctuations. To remove the effect of small local extrema, the smoothed  $A$  array is used to check the number of inflection points. The third order Savitzky-Golay filter [129] is applied to smooth the  $A$  array. The width of the smoothing window needs to be specified for the Savitzky-Golay filter to apply the smoothing. If the smoothing window size is too small, smoothing process can not remove most of the small fluctuations. In this case, some real flux ropes with small fluctuations will be discarded due to their multiple inflection points. If the smoothing window size is too large, the smoothing process will force to remove the large local extrema, which will cause the low quality structures to be labeled as flux rope candidates. After extensive experiments, we have found that the one half of the lower limit associated with each detection window width is an appropriate choice of width for its smoothing window. Because the smoothing window width in the Savitzky-Golay filter needs to be an odd number, if the one half of the lower limit is not odd, we will round it up to the nearest odd number.

The core procedure, corresponding to the inner loop denoted in Figure 3.1, consists of the following two major steps:

- **Step 1.** As the sliding detection window moves forward, we calculate the  $A$  array along the projected spacecraft path (at  $y = 0$ ) by

$$A(x, 0) = \int_0^x -B'_y(\xi, 0) d\xi. \quad (3.1)$$

Apparently the inflection point corresponds to the point along the spacecraft path where the field component  $B'_y$  changes sign and a point at which the extreme value in  $A$  is reached. If we find that the calculated  $A$  array within the window is monotonic or has more than one inflection points, we will do nothing but simply move the window forward by one data point. A monotonic  $A$  array contains no extrema and can never lead to a double-folded  $P_t$  *versus*  $A$  curve. An  $A$  array with more than one inflection points indicates that the current window may contain multiple flux rope structures. For the former situation, there is no further action needed to be done, and for the latter, a smaller size detection window in another run will take care of it. Once the  $A$  array with only one inflection point is discovered, the  $A$  array will be split into two branches at the inflection point. Then the two branches will be trimmed to have the same  $A$  values at the boundary. Note that the trimming is not according to the number of data points, but is according to the  $A$  value, because a flux rope should have the same  $A$  value at its boundary. After trimming, the two branches may not have the same lengths, but must have the same or similar boundary  $A$  values. After getting two branches of  $A$  values with the same boundary, we can calculate  $P_t$  values corresponding to each  $A$  value. With both  $P_t$  and  $A$  values obtained along the spacecraft path, we get the two branches of the  $P_t$  *versus*  $A$  curve.

- **Step 2.** The next step is to examine how well the two branches of the  $P_t$  *versus*  $A$  curve overlap. Before doing this, another check process can be performed to reduce the further workload. As a physical nature of a flux rope, the total

transverse pressure  $P_t$  must reach its maximum in the flux rope center. Reflected in the two branches of the  $P_t$  *versus*  $A$  curve, the turning point (corresponding to the inflection point in the  $B'_y$  array) must be on the top. We need to remove the cases with turning points not on top. Taking into account the measurement error and small fluctuations, we introduce the tolerance. With tolerance, we require the  $P_t$  value at the turning point be in top 15% of all  $P_t$  values. If the data segment would survive the check after undergoing all the aforementioned procedures, we are ready to obtain two more metrics as defined below to check the double-folding quality,

$$R_{dif} = \left[ \frac{1}{2N} \sum_{i=1}^N ((P_t)_i^{1st} - (P_t)_i^{2nd})^2 \right]^{\frac{1}{2}} / |\max(P_t) - \min(P_t)|, \quad (3.2)$$

and

$$R_{fit} = \left[ \frac{1}{L} \sum_{i=1}^L (P_t(x_i, 0) - P_t(A(x_i, 0)))^2 \right]^{\frac{1}{2}} / |\max(P_t) - \min(P_t)|. \quad (3.3)$$

We determined that  $R_{dif} \leq 0.12$  and  $R_{fit} \leq 0.14$  could guarantee good flux rope quality while keeping as many candidates as possible.

Equation (3.2) is modified from Equation (5) in Hu and Sonnerup's paper [111], and Equation (3.3) is taken from Hu et al.'s paper [115].  $R_{dif}$  represents the difference between two branches, in which both  $(P_t)_i^{1st}$  and  $(P_t)_i^{2nd}$  are calculated from observational data. We find the  $A$  array and the corresponding  $P_t$  array in the first branch, then use these  $A$  values to look up the corresponding  $P_t$  in the second

branch. If there is no correspondence in the second branch for some points in the first branch, we use linear interpolation to create a match. Then we repeat the same process for the second branch. Finally, each  $P_t$  in one branch has a counterpart in the other branch. We insert the two interpolated  $P_t$  arrays into Equation (3.2) to calculate  $R_{dif}$ . Only  $R_{dif}$  alone is not sufficient to decide if a segment of data is a good flux rope candidate or not, because a small  $R_{dif}$  can only guarantee the good double-folding of the two branches of  $P_t$  *versus*  $A$  curve, no matter what the shape of the folded curve is. A reliable threshold for  $R_{dif}$  is hard to set for acceptable flux rope candidates. To help with this, we obtain an additional fitting residue by using a 3rd order polynomial to fit the data points of  $P_t$  *versus*  $A$ . This fitting ignores the time sequence of the data points and merges two branches into one. Its fitting residue is defined in Equation (3.3) and denoted as  $R_{fit}$ , where  $P_t(x_i, 0)$  is calculated from measured data and  $P_t(A(x_i, 0))$  is calculated from the fitting function. Note that there is a fraction factor  $1/2N$  in  $R_{dif}$ 's definition, but in  $R_{fit}$ 's definition, this factor is  $1/L$ . This is because in  $R_{dif}$ , the number of terms under the summation operator is only half of the number in  $R_{fit}$ , if the two branches of  $P_t$  *versus*  $A$  curve have the same number of data points. We use two different factors to make the two metrics,  $R_{dif}$  and  $R_{fit}$ , comparable in magnitude. However, the two branches of  $P_t$  *versus*  $A$  curves must have the same  $A$  value range, but not necessarily have the same number of data points. In practice, even with the inclusion of these fractional factors, we still set different threshold values for  $R_{dif}$  and  $R_{fit}$ . Besides the number of data points, the range of  $P_t$  value may also affect  $R_{dif}$  and  $R_{fit}$ . So we normalize  $R_{dif}$  and  $R_{fit}$  by the range  $|\max(P_t) - \min(P_t)|$ . In the flux rope searching process, we

use only  $R_{dif}$  to look for optimal  $z$ -axis orientation. For a given data segment, the  $R_{dif}$  for each trial  $z$ -axis orientation is calculated, then the  $z$ -axis orientation with the minimum  $R_{dif}$  is taken as the optimal axial orientation. With the determined optimal axial orientation, if both  $R_{dif}$  and  $R_{fit}$  satisfy our criteria, this data segment will be labeled as a flux rope candidate. The threshold values of  $R_{dif}$  and  $R_{fit}$  are selected based on examining thousands of data segments with double-folding features in  $P_t(A)$ , and are given in Table 3.1.

### 3.2 Cleanup and Post-Processing

When a sliding window process is finished, we will get a record list of identified flux rope intervals. However, this record list has many overlapped records or intervals. We use an example to illustrate why overlapping happens. We imagine a true flux rope starting from 8:00 am and ending at 10:00 am. When a sliding window with the width of 2 hours just covers the entire flux rope time range, this flux rope will be recognized and recorded. If the window moves forward and covers the time range from 8:05 am to 10:05 am, the detection algorithm will likely recognize a flux rope from 8:05 am to 9:55 am (after trimming the two branches of  $P_t$  versus  $A$  curve). As the window moves on by one data point each time, as long as it still covers the turn point of the flux rope from 8:00 am to 10:00 am (the largest flux rope), and the detected flux rope duration is longer than the lower limit, the program will pick a part of the largest flux rope as a new flux rope. These flux ropes share the same turn point, and we call them a flux rope cluster. To clean up such a cluster from the record list, we usually pick the interval with the smallest  $R_{dif}$  values and discard

the others. We have considered possible improvements to avoid the overlapping. One possible method is to move the entire sliding window out of the time range of a flux rope once it is detected. However, we cannot guarantee that the one we picked is the best one in a flux rope cluster. Eventually we decided to slide the detection window continuously to guarantee the detection of the maximum number of flux ropes.

Even after we clean up the flux rope clusters, there may still exist overlapped flux ropes, which do not share the exactly same turn point, but these turn points are very close to each other. Due to the error and small fluctuation of observational data, even for the same flux rope, if we change the beginning time and end time a little bit, the detection algorithm may give us a little bit different axial orientation and  $P_t$  versus  $A$  turn point. This kind of overlap also needs to be cleaned up. We group the flux ropes with similar turn points into one flux rope cluster, then we keep the one with the minimum  $R_{dif}$  and discard the others. As for the selection criteria of similar turn points, we set different tolerance value for flux ropes with different sizes. For the flux ropes with time duration longer than 1 hour, we consider the flux ropes as identical ones when the turn point time differences are less than 10 minutes. For the flux ropes with time duration less than 1 hour, we set the tolerance to 5 minutes. So far, we have combined the flux rope records which are considered identical. However, this is not the end of the cleanup process yet. Now we may still have overlaps sharing the same flux rope boundary. We still use an example to explain this situation. If we already have a flux rope starting from 8:00 am and ending at 10:00 am, with the  $z$ -axis orientation  $(\theta, \phi)$ , it may just so happen that the detection algorithm finds another flux rope starting from 9:50 am and ending at 11:50 am, with a different  $z$ -axis orientation  $(\theta, \phi)$ .

axis orientation  $(\theta', \phi')$ . The question is: which one should be kept? The answer will be very simple if we just set one sliding window width and run one iteration. We can simply keep the one with the smaller  $R_{dif}$  or  $R_{fit}$ . Or we can check the other criteria and keep the better one. We can even trim the overlapped part and keep both. When we set multiple sliding window widths and run multiple iterations, we will end up with multiple flux rope record lists with different lower and upper size limits. Imagine that we have list 1 which contains the flux rope records with time durations longer than 100 minutes (lower limit) but shorter than or equal to 120 minutes (upper limit), and we also have list 2 which contains the flux rope records with time durations between 160 minutes and 180 minutes. Suppose that in list 1, we could have two records: one record is from 8:00 am to 10:00 am, and the other record is from 9:50 am to 11:50 am. In list 2, we could have a record from 6:00 am to 9:00 am. If, by any chance, we kept the one from 8:00 am to 10:00 am and discarded the one from 9:50 am to 11:50 am, when we merge the remaining one in list 1 (from 8:00 am to 10:00 am) to list 2, we would still have overlapping. If we find that the one in list 2 (from 6:00 am to 9:00 am) has the higher quality than the one kept in list 1, we will discard the one in list 1. Finally, we may discard both records in list 1. As a matter of fact, if otherwise the one from 9:50 am to 11:50 am in list 1 is a flux rope with good quality, we could have kept it as well as the one in list 2 (there is no overlapping between intervals 9:50 am-11:50 am and 6:00 am-9:00 am). In what follows, we will further explain the reason why we use multiple window widths strategy and discuss how to combine the flux rope record lists with different sliding window widths.

When all iterations with different window widths are finished, we need to combine all flux rope records. With the program setting introduced in the beginning of Section 3.1, we will end up with 70 event lists from 70 iterations. We cannot simply merge these lists into one, since a long flux rope may cover one or more short flux ropes from different lists. In fact, this is an interval scheduling problem in computer science. The optimal solution is to accommodate as many flux rope records as possible. We use the greedy algorithm to find the optimal solution. The main idea of the greedy algorithm in interval scheduling problem is to firstly accommodate the event with the earliest finishing time. The procedures are the following: 1) clean the overlapped records in the event list with the longest flux rope duration. We sort the records by the flux rope end time. Firstly, find all the flux ropes that overlap with the first record, then keep the first flux rope and discard others. Then process the next record until all overlapped records are removed. 2) Find all the slots in the temporary list. Then we pick the suitable records from the event list with the second longest flux rope duration, and insert it into the slots. Each slot may contain some overlapping flux ropes. We still use the greedy algorithm to accommodate them. 3) Continue with the next longest, and so on, until all flux ropes are accommodated.

The last check step is the standard Walén test to rule out possible Alfvénic structures [130]. An Alfvén wave structure may show the similar magnetic field profile in the GSE coordinate system. The scale size of small flux ropes is comparable with that of Alfvén wave structures. We have to do further test to remove Alfvén waves from our flux rope database. We remove the records whose absolute value of Walén test slope is greater than or equal to 0.3 (indicating significant remaining flows in

deHoffmann-Teller frame). Up to this point, we have finished all major steps to build the flux rope database. At last, we have the option to apply one more criterion. Because the average magnitude of magnetic field in the ambient solar wind is about  $5 \text{ nT}$ , we remove the flux rope records whose average magnitude of magnetic field is less than  $5 \text{ nT}$ .

At the end of this section, we explain the reason why we expand the upper and lower limit of each iteration by 1 minute. In the cleanup and post-processing step, because the shorter flux rope candidates tend to have smaller  $R_{dif}$  and  $R_{fit}$ , the cleanup algorithm tends to keep the flux ropes with shorter duration in each bin. As a result, in the duration histogram, the flux ropes tend to accumulate near the lower limit of each bin. We extend the boundaries of each bin to make overlaps to reduce this accumulation effect. In fact, it won't make much difference if we extend the boundaries of a flux rope by either 2 or 3 minutes. Since the bin width that we use is narrow (only 5 minutes), we can just simply treat the flux ropes with different durations in the same bin as the same duration flux ropes. In practice, extending the boundaries of each bin has reduced the accumulation effect.

In summary, Table 3.1 lists the set of metrics and criteria we use in the identification of small-scale flux rope events from the in-situ solar wind observations. The duration  $9 \sim 361$  minutes covers the range of most small scale flux ropes, and this range can be easily extended to intermediate or large size flux ropes,  $6 \sim 12$  hours, bridging the gap between small-scale flux ropes and MCs. The criterion  $|\bar{B}| \geq 5 \text{ nT}$  excludes small fluctuations in the solar wind. The metrics  $R_{dif}$  and  $R_{fit}$  guarantee the

good quality of small-scale flux ropes. And the Walén test slope of small magnitude,  $\leq 0.3$  removes the Alfvénic structures.

**Table 3.1:** Small-scale Magnetic Flux Rope Detection Metrics and Criteria

Duration	$ \bar{B} $	$R_{dif}$	$R_{fit}$	Walén test slope
$9 \sim 361$ (minutes)	$\geq 5$ (nT)	$\leq 0.12$	$\leq 0.14$	$\leq 0.3$

### 3.3 Online Database of Small-scale Magnetic Flux Ropes

We apply the flux rope detection algorithm based on the GS reconstruction technique to the Wind spacecraft measurements during  $1996 \sim 2016$ , covering nearly two solar cycles. We successfully detected a large number of small-scale magnetic flux ropes with more general configurations, including non-force-free and non-axisymmetric configurations. Table 3.2 lists the number of flux rope detected by our algorithm in each year. There are a total number of 74,241 small-scale magnetic flux ropes detected, with an average number more than 3,500 per year. This database provides sufficient number of samples for researcher to carry out statistical analysis, correlate with other structures, and examine some special cases in detail.

**Table 3.2:** The Number of Detected Small-scale Magnetic Flux Ropes in Each Year

Year	1996	1997	1998	1999	2000	2001	2002	2003	2004	2005	2006
Counts	2787	2878	4182	4454	4425	4203	5930	6086	4229	4017	2620
Year	2007	2008	2009	2010	2011	2012	2013	2014	2015	2016	<b>Total</b>
Counts	2040	1620	1076	2209	2731	3051	2658	3690	4987	4368	<b>74241</b>

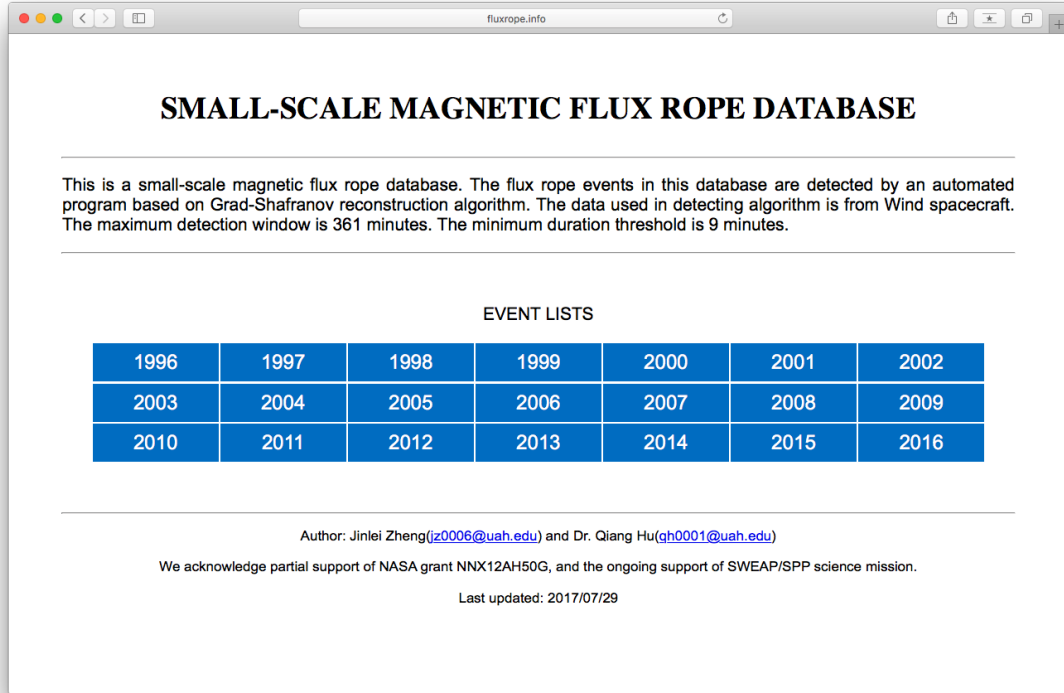


**Figure 3.2:** The home page of the small-scale magnetic flux rope database website.

We have established a website (<https://fluxrope.info>) to host this database online. We make the database open to public and keep it up to date. More flux rope cases with longer durations and at higher latitude locations will be added in near future. Figure 3.2 is the home page of the small-scale magnetic flux rope database website. When clicking on any year on the “EVENT LISTS” table, the annual event list page will show up, which is presented in Figure 3.3 for year 1996. The event list page lists every detected flux rope event in one year in chronological order. For each flux rope record in each row, some basic characteristics are listed such as time range in UT, duration in minutes, fitting residue ( $R_{fit}$ ), average magnetic field strength,

fluxrope.info/1996/year1996.html

HOME ← →

**Small-scale Flux Rope Events in 1996**

No.	Time Range	Duration	Residue	$\langle B \rangle$ (nT)	$B_{\max}$ (nT)	$\langle \beta \rangle, \langle \beta_p \rangle$	$\langle V_{sw} \rangle$ (km/s)	$\langle T_p \rangle$ ( $10^6$ K)	Orientation
1	<a href="#">1996/01/01 02:01 ~ 1996/01/01 02:56</a>	56	0.1017	5.25	6.04	nan, 1.01	388	0.10	0=60, $\phi=340$
2	<a href="#">1996/01/01 03:27 ~ 1996/01/01 03:59</a>	33	0.1284	5.47	6.00	nan, 0.65	388	0.09	0=20, $\phi=220$
3	<a href="#">1996/01/01 05:07 ~ 1996/01/01 05:45</a>	39	0.1127	5.37	6.12	nan, 0.85	387	0.09	0=50, $\phi=340$
4	<a href="#">1996/01/01 05:47 ~ 1996/01/01 06:56</a>	70	0.1336	5.42	6.25	nan, 0.91	389	0.08	0=50, $\phi=280$
5	<a href="#">1996/01/01 08:51 ~ 1996/01/01 09:37</a>	47	0.1293	5.07	6.02	nan, 1.42	407	0.08	0=70, $\phi=0$
6	<a href="#">1996/01/01 09:40 ~ 1996/01/01 09:51</a>	12	0.0812	5.17	5.79	nan, 1.05	409	0.07	0=10, $\phi=40$
7	<a href="#">1996/01/01 10:34 ~ 1996/01/01 10:53</a>	20	0.1320	6.70	6.94	nan, 0.23	414	0.04	0=50, $\phi=80$
8	<a href="#">1996/01/01 11:39 ~ 1996/01/01 11:52</a>	14	0.1098	5.60	5.89	nan, 0.58	411	0.06	0=60, $\phi=80$
9	<a href="#">1996/01/01 11:54 ~ 1996/01/01 12:02</a>	9	0.1040	5.58	6.39	nan, 0.64	409	0.07	0=70, $\phi=280$
10	<a href="#">1996/01/01 12:09 ~ 1996/01/01 12:35</a>	27	0.0903	5.74	6.16	nan, 0.61	407	0.07	0=80, $\phi=240$
11	<a href="#">1996/01/02 14:24 ~ 1996/01/02 14:42</a>	19	0.0939	5.90	6.17	nan, 0.49	377	0.07	0=10, $\phi=260$
12	<a href="#">1996/01/02 17:58 ~ 1996/01/02 18:06</a>	9	0.0564	7.73	9.16	nan, 0.55	386	0.07	0=80, $\phi=320$
13	<a href="#">1996/01/02 18:15 ~ 1996/01/02 18:23</a>	9	0.1045	6.97	7.74	nan, 0.95	396	0.09	0=60, $\phi=280$
14	<a href="#">1996/01/02 18:24 ~ 1996/01/02 20:24</a>	121	0.1343	9.49	11.70	nan, 0.37	425	0.09	0=70, $\phi=280$
15	<a href="#">1996/01/02 20:44 ~ 1996/01/02 20:57</a>	14	0.0699	8.80	9.99	nan, 0.70	480	0.15	0=50, $\phi=120$
16	<a href="#">1996/01/02 20:59 ~ 1996/01/02 21:07</a>	9	0.0733	5.55	6.50	nan, 3.56	491	0.28	0=20, $\phi=320$
17	<a href="#">1996/01/02 21:07 ~ 1996/01/02 21:17</a>	11	0.0571	6.03	7.33	nan, 2.65	491	0.26	0=60, $\phi=20$
18	<a href="#">1996/01/02 21:48 ~ 1996/01/02 22:09</a>	22	0.1045	6.78	7.53	nan, 1.22	459	0.21	0=80, $\phi=160$
19	<a href="#">1996/01/02 22:25 ~ 1996/01/02 22:33</a>	9	0.0830	6.32	6.74	nan, 1.48	476	0.23	0=70, $\phi=40$
20	<a href="#">1996/01/03 00:39 ~ 1996/01/03 00:53</a>	15	0.1056	5.72	6.37	nan, 1.53	489	0.19	0=80, $\phi=100$
21	<a href="#">1996/01/03 02:50 ~ 1996/01/03 02:59</a>	10	0.1296	6.28	6.66	nan, 1.19	466	0.19	0=60, $\phi=120$
22	<a href="#">1996/01/03 03:27 ~ 1996/01/03 04:41</a>	75	0.1149	6.82	7.99	nan, 0.77	456	0.15	0=20, $\phi=100$
23	<a href="#">1996/01/03 04:41 ~ 1996/01/03 04:50</a>	10	0.1152	7.67	7.98	nan, 0.34	458	0.10	0=10, $\phi=160$
24	<a href="#">1996/01/03 04:51 ~ 1996/01/03 05:32</a>	42	0.1253	7.70	8.06	nan, 0.33	460	0.09	0=30, $\phi=20$

**Figure 3.3:** The annual event list page of the small-scale magnetic flux rope database website.

maximum magnetic field strength, average plasma  $\beta$ , average proton plasma  $\beta_p$ , average solar wind speed, average proton temperature, and flux rope axial orientation. More information on magnetic field and plasma profiles is stored in the database and can be put online in new versions of the website. These quantities make it very convenient for us and other researchers to further apply more selection criteria to pick desirable subset of events for different purposes.

The time range for each record is a clickable hyperlink which will navigate to the detailed flux rope information page which is demonstrated in Figure 3.4 and Figure 3.5 for one particular event. Figure 3.4 shows the upper part of an event page

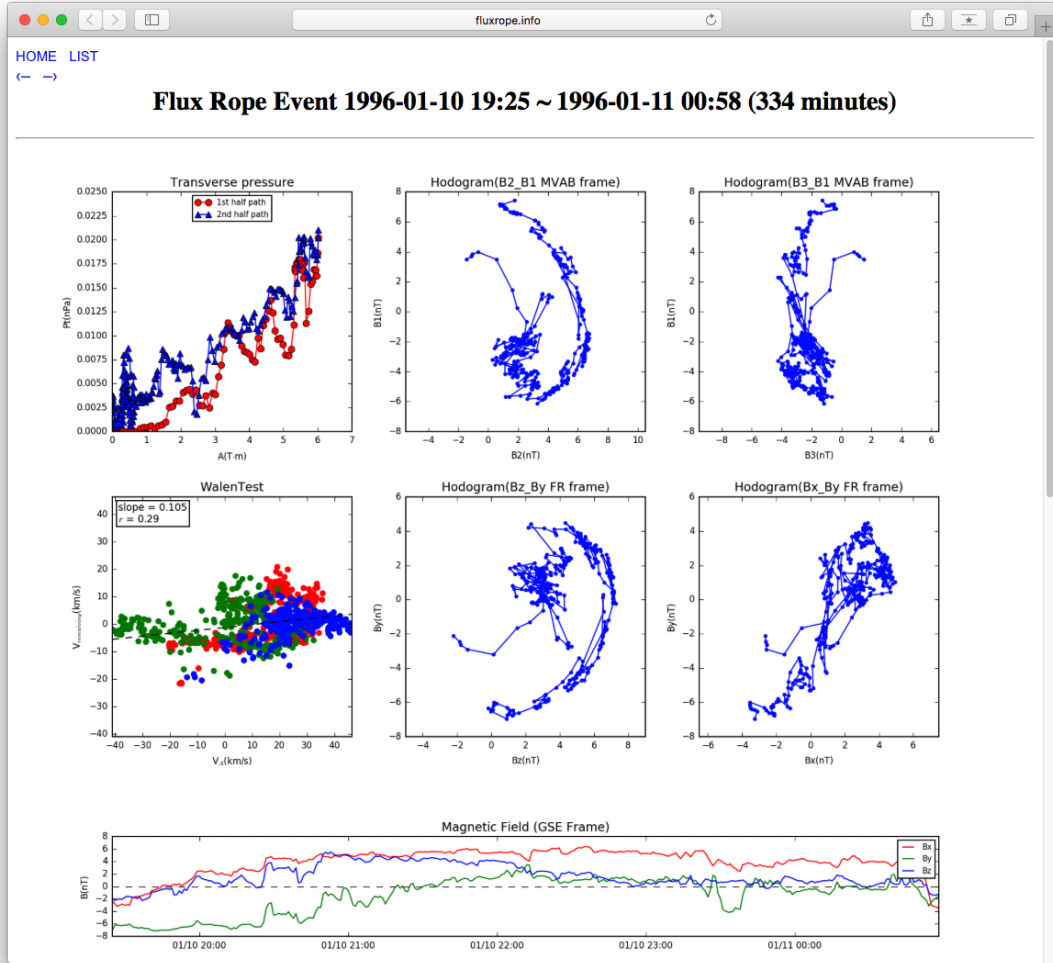


**Figure 3.4:** Detailed information for one small-scale magnetic flux rope record: event page part 1.

and Figure 3.5 shows the lower part of an event page. In Figure 3.4, the upper panel in the first column is the plot of  $P_t$  versus  $A$ , from which one can easily judge the double-folding quality of  $P_t(A)$ , a necessary condition for being a flux rope. The lower panel in the first column is the plot of Walén test with the slope and correlation coefficient shown on the plot. From these two quantities one can know the magnitude of the

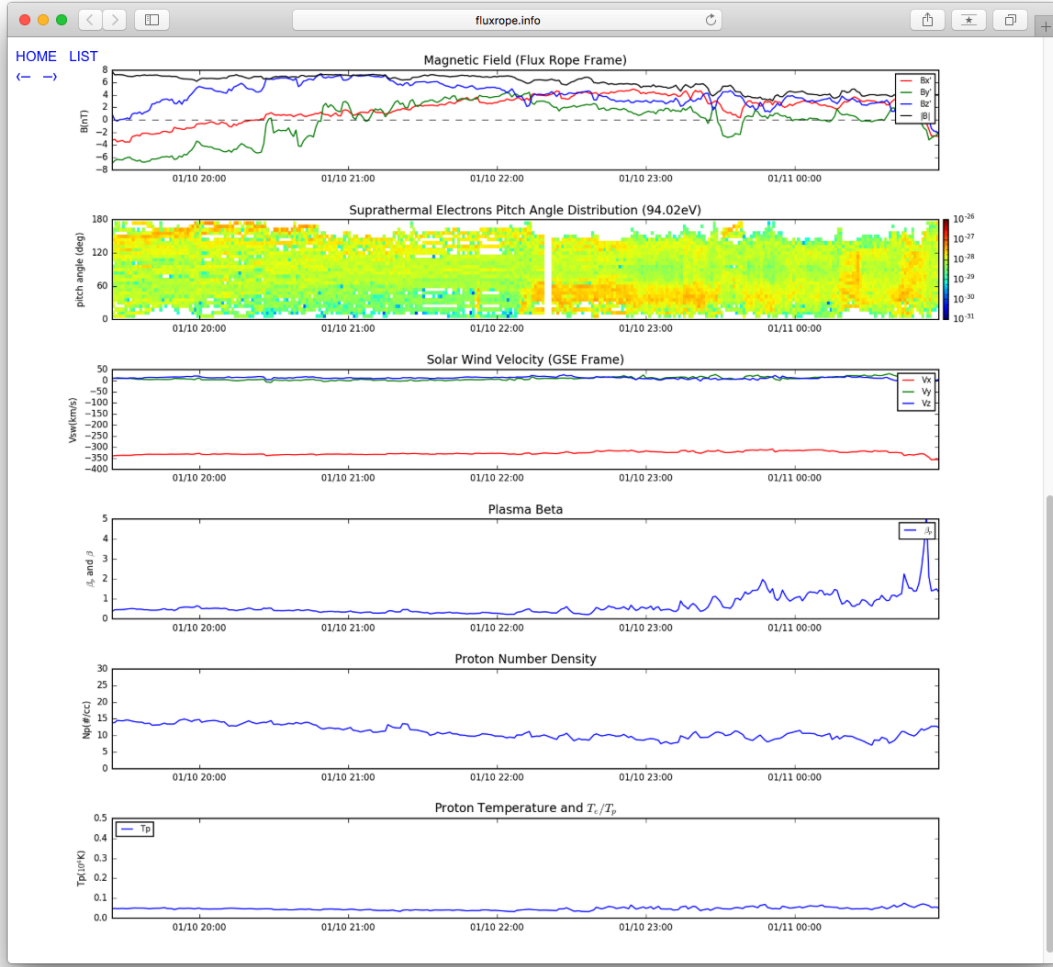


**Figure 3.5:** Detailed information for one small-scale magnetic flux rope record: event page part 2.

remaining flows for each velocity component in the deHoffmann-Teller (HT) frame.

Generally speaking, a spread of the data points horizontally indicates satisfaction of the detection criterion based on the Walén test. In the second and the third columns, the upper panels are the hodograms of the flux rope magnetic field components in the MVAB frame and the lower panels are the hodograms of the flux rope magnetic field

components in the flux rope reconstruction frame. The movement of the end points of magnetic field vectors is displayed in these hodograms. Generally a smooth rotation in one or two magnetic field components, typical of a flux rope configuration, may be visualized in these plots. The other panels in Figure 3.4 and Figure 3.5 are time series data of magnetic field and plasma parameters, including the pitch angle distribution of suprathermal electrons, the temperature of protons and electrons, plasma beta, etc.

This website provides a large number of small-scale magnetic flux rope events and lots of essential information, which can benefit the relevant studies on small-scale magnetic flux ropes in the solar wind. Beginning with the next chapter, we will make use of this database to perform statistical analysis as well as detailed case studies. We will present the fruitful outcomes from this database and will anticipate further development and usage of this database in future work.